Revisiting bathymetry dynamics in Lake Urmia using extensive field data and high-resolution satellite imagery

Mohammad Danesh-Yazdi [a,*], Majid Bayati [a], Massoud Tajrishy [a,b], Behdad Chehrenegar [c]

[a] Department of Civil Engineering, Sharif University of Technology, Azadi Avenue, Tehran, Iran
[b] Remote Sensing Research Center, Sharif University of Technology, Azadi Avenue, Tehran, Iran
[c] Head of Research Division at Urmia Lake Restoration Program, Tehran, Iran

ARTICLE INFO

ABSTRACT

Bathymetric mapping for an accurate estimation of stored water volume in drying lakes is a key information for an effective monitoring of their recession or restoration status. Extraction of bathymetry in shallow saline lakes using remote sensing techniques has always been challenging due to the complex influences imposed by the physical properties of substrate and the spatial variability of salinity. In this study, we developed a machine learning-based model to quantify the implicit, non-linear relationship between water depth and surface reflectance by leveraging extensive in-situ data and high-resolution satellite imagery. We trained and tested the learning model in the hyper-saline Lake Urmia (LU), which faced catastrophic drying over the past two decades. To this end, we used Landsat-8 imagery and 32,984 hydrography data points surveyed by the Urmia Lake Restoration Program (ULRP) from 2017 to 2020 during six stages. To enhance the model accuracy, we tuned the model inputs by optimizing the spectral information and clustering in-situ data from stages with similar meteorological conditions into three classes. The results demonstrated the high accuracy of the developed intelligent model as evidenced by $R^2 = 0.8 \sim 0.9$ and RMSE = $7.8 \sim 17.9$ cm for the three models. We found that the average water depth in the LU was increased from 0.43 m in September 2018 to 2.00 m in May 2020. In particular, the lake water volume in May 2020 was 3.6 times greater than that in February 2019, which marks a remarkable shift in the LU restoration. Dynamic bathymetric maps also witnessed considerable salt dissolution taking place across the lake during this period. Finally, we extracted the LU level-area relationship by processing 172 Landsat images between 1984 and 2020, which was validated against the field data surveyed along the lake water boundary in 2019. The results indicated that the level-area relationship follows a dual linear relationship separated at the water level of 1271.31 m.

1. Introduction

Many saline lakes worldwide have faced drastic desiccation over the past decades, e.g., Walker Lake in Nevada, USA (Benson et al., 1991), Aral Sea in Central Asia (Micklin, 2007; Micklin, 1988), Great Salt Lake in Utah, USA (Bedford, 2009), and Lake Urmia in Iran (AghaKouchak et al., 2015), among others. Anthropogenic activities such as extensive agriculture development than climate variability have witnessed a much greater contribution to the drying of these lakes (Wurtsbaugh et al., 2017). Having caused serious adverse impacts on water quality (Bayati and Danesh-Yazdi, 2021), human health (Sadeghi-Bazargani et al., 2019), and biota diversity (Stenger-Kovács et al., 2014), implementation of restoration activities is indispensable to guarantee the long-term sustainability of these environments. Continuous monitoring of water storage in a reviving lake is the most reliable tool to assess the success of the employed restoration plans.

Estimating water balance components, i.e., direct precipitation on the lake, evaporation rate, and inflows from and outflows to surface and groundwater, can yield the change in water storage. However, this is often challenging due to the complexity and uncertainty involved in estimating these variables by empirical relationships or numerical models using ground measurements and/or space-borne data (Gronewold et al., 2020; Winter, 1981). Alternatively, we can directly estimate the stored water volume of an aquatic system from its geometry given the underlying bed topography called bathymetry. The bathymetry of saline lakes can be highly dynamic in both space and time due to the

---

fluctuating rates of salt precipitation and dissolution. As such, recursive bathymetric delineation of these environments is necessary for an appropriate estimation of their stored water volume over time.

We can derive bathymetric maps traditionally by shipboard acoustic echo-sounding using single or multi-beam sonar. Despite its high accuracy, this technique is costly, time-consuming, and labor-intensive, especially for surveying shallow waters due to the decreased swath width (Dierssen and Theberge, 2014). Instead, active and passive remote sensing (RS) contextualized into imaging and non-imaging methods have been widely used to extract bathymetric maps (e.g., Bian et al., 2018; Cahalane et al., 2019; Gao, 2009; Stewart et al., 2016). In contrast to traditional approaches, RS has facilitated a fast, low-cost, and extended spatial coverage over areas that may not be accessible for ground measurements. The most common sensing techniques for bathymetry derivation are based on optical RS (i.e., multispectral or hyperspectral imagery) (e.g., Klonowski, 2007; Ma et al., 2020; Pacheco et al., 2015), Light Detection and Ranging (LiDAR) (e.g., Li et al., 2019; Xu et al., 2020), satellite altimetry (e.g., Smith et al., 2005; Smith and Sandwell, 1994), and Synthetic Aperture Radar (SAR) (e.g, Bian et al., 2018; Stewart et al., 2016). Subsequently, a number of methods have been developed for deriving bathymetry information using RS data captured by the above techniques. In particular, the models based on optical RS, e.g., the Lyzenga model (Lyzenga, 1978; Lyzenga, 1985; Lyzenga et al., 2006), the Jupp model (Jupp, 1988), and the Stumpf model (Stumpf et al., 2003), hold the most frequent applications over a variety of water bodies.

Former extensive studies have shown that the accuracy of water depth (H) estimation from these algorithms depends strongly on the heterogeneity in water turbidity, reflective properties of substrate, and water depth variation (see Jawak et al. (2015) and referenced therein for a comprehensive review of the accuracy, advantages, drawbacks, and the domain of applicability of these models). Here, we further argue that in addition to the underlying assumptions of the above models, their simple linear or ratio transform structure cannot adequately explain the integrated influence of the physical properties of water and substrate across an image extent. In addition, these algorithms typically use a fraction of spectral information available from airborne data. To tackle these limitations, we can leverage fine-tuned machine learning algorithms to develop non-linear relationships between multi-spectral data and in-situ measurements of water depth under a wide range of conditions. These algorithms include, but are not limited to, Artificial Neural Networks (ANN) (Ceyhun and Yalçın, 2010; Gholamalifard et al., 2013; Liu et al., 2018; Moses et al., 2013; Sandidge and Holyer, 1998), Random Forest (Manessa et al., 2016; Sagawa et al., 2019; Yunus et al., 2019), Support Vector Machine (Misra et al., 2018; Wang et al., 2019), and Ensemble Regression Trees using Bootstrap Aggregation and Least Squares Boosting (Mohamed et al., 2017). The findings of these studies unanimously demonstrate that machine learning-based algorithms show an improved performance in deriving bathymetric maps as compared to those obtained by other traditional approaches.

In this study, we developed a learning-based model to decipher the dynamics of bathymetry in the reviving, hyper-saline shallow Lake Urmia (LU) located in northwestern, Iran. To the best of our knowledge, this is the first study that leveraged the most recent extensive in-situ hydrography measurements to derive bathymetric maps between 2017 and 2020. Regarding the outdated bathymetry being currently used to monitor the lake water volume, the new findings yield a more reliable insight into evaluating the restoration status of LU over the recent years. We further present the most updated level-area relationship in the LU by extracting the lake surface area with the aid of high-resolution satellite imagery between 1984 and 2020. We validated the employed classification algorithm against the lake boundary data surveyed at multiple traces in 2019. In contrast to previous studies, the developed level-area-volume relationship describes the most dry and wet conditions of the lake during the last 50 years.

The rest of this article is organized as follows. Section 2 presents the study area and describes the in-situ measurements and RS data used for the purpose of this study. In this section, we also outline the methodology to map bathymetry. Section 3 presents the results, and Section 4 discusses the findings by focusing on (i) the revisited level-area-volume relationship in the LU, (ii) the influence of bathymetry and RS data quality on the accuracy of the water depth prediction model, and (iii) the dynamics of salt precipitation and dissolution in the LU. Finally, Section 5 concludes with the study findings.

2. Methods and data

2.1. Study area

LU is located in the northwest of Iran (37° 04′ N to 38° 16′ N, 45° 02′ E to 46° 00′ E), which receives freshwater from several rivers draining twelve sub-basins in the ~52,000 km² Lake Urmia Basin (Fig. 1a). Registered as a Protected Area (1967), a National Park (1971), a Ramsar Site (1975) and a UNESCO Biosphere Reserve (1976), LU is recognized as one of the wetlands of international importance. It is also well-known for its hyper-salinity where the salt concentration has recorded fluctuations between 140 g/l and 380 g/l (Zeinoddini et al., 2009). Recent field investigations of the lake sedimentology reveal salt deposits on the lake bottom (Fig. 1e) ranging a few centimeters in the south up to three meters in the north (Lahijani et al., 2020). LU is partly separated by the 15 km Kalantari Causeway and Bridge (Fig. 1b), which has intervened the water circulation and mixing between the northern and southern parts. The intra-annual variation of salinity across the LU demonstrates two patterns of salinity distribution. While the distribution of salinity concentration in the southern and northern parts becomes distinct in high-flow months, a relatively uniform distribution is observed during dry months across the whole LU (Bayati and Danesh-Yazdi, 2021).

Historical record of the LU water level (H) indicates that the lake lost about eight meters of water between 1996 and 2016 (Fig. 1f), which was equivalent to a loss of ~33 BCM of water. Several former studies have pointed out the major reasons for the drastic decline of LU. They include intensive agricultural development, the imbalance between water supply and demand, decreased environmental flow by the improper operation of reservoirs, illegal withdrawal from surface and groundwater resources, and low irrigation efficiency in the Lake Urmia Basin. This mostly human-made shrinkage led to a wide range of environmental and socioeconomic problems such as desertification, increased soil salinity in the agricultural areas near the lake, disturbance in the ecological condition of the lake biota (e.g., Artemia), and increased unemployment rate due to recession in agricultural activities (see Danesh-Yazdi and Ataie-Ashtiani (2019) and references therein).

To cease the drying trend of LU, Urmia Lake Restoration National Committee has planned and implemented several basin management practices to increase inflow into the LU since 2013. Reducing agriculture water allocation, stream dredging to increase the delivering capacity of the rivers feeding the lake (Fig. 1c), and artificial channelization in the southern sub-basins of the lake, which provide more than 50% of the lake annual inflow (Fig. 1d), are among such actions (Urmia Lake Restoration Program (ULRP), 2018). As a result, the streamflow rate into the lake is supposed to increase and cause enhanced sediment yield accordingly, which is spatially variable depending on the sediment rating curve of each river flowing into the lake. Moreover, the increased volume of freshwater flow leads to salt dissolution in high-flow seasons especially near the inlet zones, while salt precipitation dominates in the dry seasons with spatiotemporally different rates. The interplay between sedimentation, salt precipitation, and salt dissolution processes makes the lakebed topography dynamic, which clearly changes the lake level-volume relationship over time.

2.2. Hydrography data

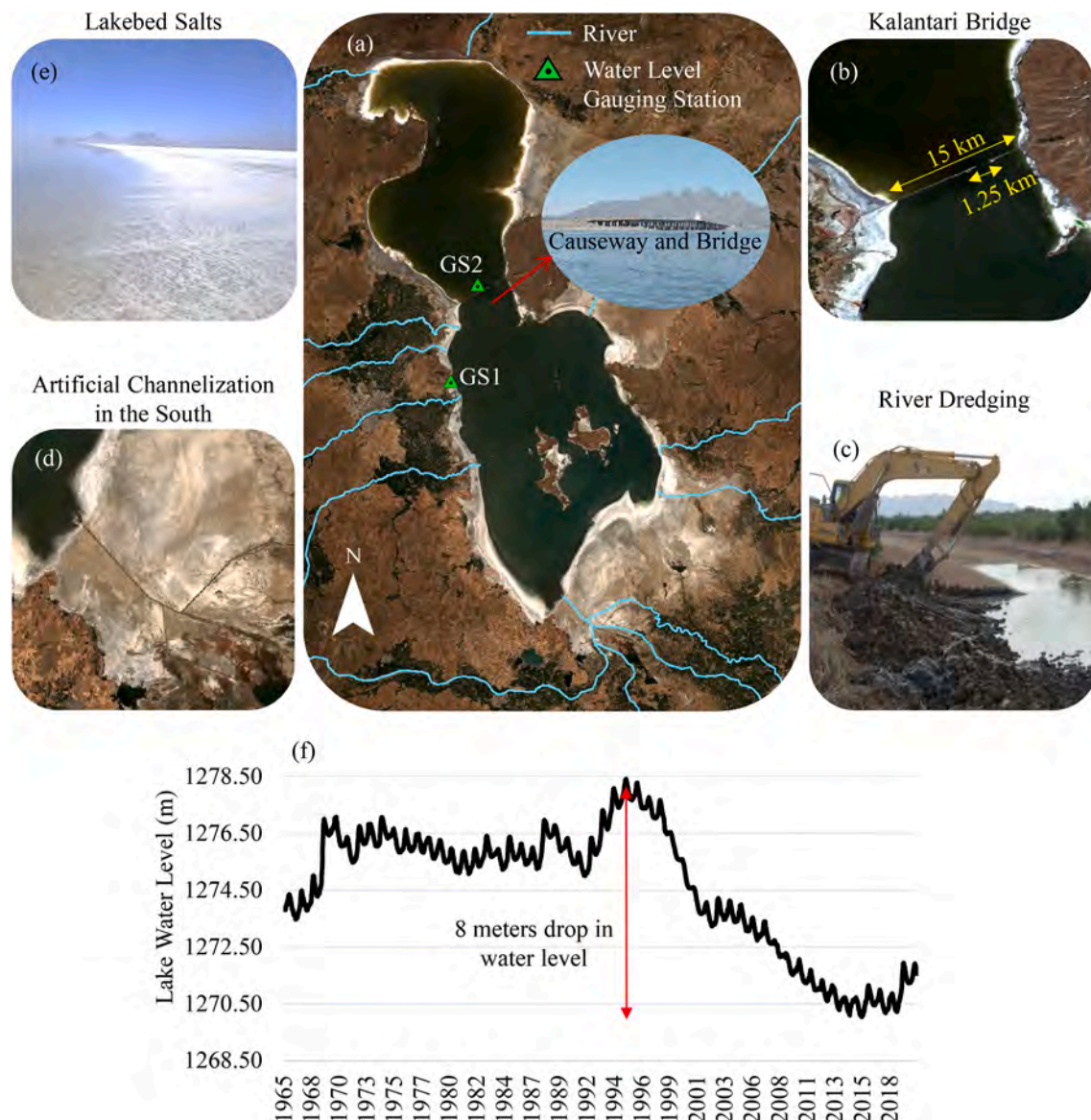We used hydrography data collected from six surveys that were

Fig. 1. Human-induced changes in Lake Urmia (LU) region. Panel (a) illustrates the Landsat imagery of the LU. The main feeding rivers, the geographical location of the lake level gauging station (GS1 and GS2), and the location of middle causeway are shown. Panel (b) indicates the extent of the causeway and its opening length. Panel (c) shows an example of river dredging operations in the Lake Urmia Basin to enhance the carrying capacity of streams. Panel (d) shows the artificial channelization in the southwestern LU to facilitate increased inflow to the lake. Panel (e) indicates the salty lakebed. The time series of lake level fluctuations between 1965 and 2020 is shown in panel (f).

carried out by multiple sources between September 2017 and May 2020. Table 1 gives the date, location and source of the surveyed data. The Iranian Institute of Space Research Mechanics (ISRC) carried out the first to fifth surveys during September 23–October 22, 2017; March 6–April 20, 2018; July 7–September 9, 2018; September 23–December 21, 2018; and February 24–March 16, 2019, respectively, in which water depth at 4894, 6273, 684, 1629, and 8485 points were surveyed using a combination of echo-sounder and RTK GPS. The first, second, and fourth surveys were conducted along 12 paths of 10 km (separated by 500 m) centered on the Kalantari Causeway. In the third and fifth surveys, data were collected along 12 and 24 paths with different lengths across the whole lake, respectively. The sixth survey was operated by the Darya Naghsheh Consulting Engineers during May 17–May 27, 2020, by which 11,019 points were surveyed by an echo-sounder across the whole lake. We received the raw hydrography data mentioned above from the Urmia Lake Restoration Program (ULRP).

To compute the lakebed elevation from the measured H data, we used daily H data recorded by a hydrostatic recording gauge at the Golmankhaneh station. This station was originally located on the Mid-western shore of the LU (37° 36′ 03″ N, 45° 15′ 31″ E) (GS1 in Fig. 1a). However, due to the lake level fall, the station was relocated to the lake center near the Kalantari Bridge (37° 47′ 26″ N, 45° 22′ 07″ E) in August 2008 (GS2 in Fig. 1a).

2.3. Satellite data

We used Landsat 4–5 TM Collection 2 Level-2 and Landsat-8 OLI/TIRS Collection 2 Level-2 products to delineate the LU surface area from 1984 to 2020. We derived the bathymetric maps from 2017 to 2020 using Landsat-8 imagery. Level-2 products give surface reflectance values that already corrects the effects of atmospheric scattering and absorption (Landsat collection 2, 2021). For each period during which hydrography data were collected, we downloaded a satellite image from USGS Earth Explorer. If a cloud-free image was not available in a survey

Table 1
The date, location and source of hydrography data.

Survey	Survey Location	Survey Period	Survey Source
1	4894 points along 12 paths of 10 km (separated by 500 m) centered on the Kalantari Causeway.	September 23–October 22, 2017	Iranian Institute of Space Research Mechanics (ISRC)
2	6273 points along 12 paths of 10 km (separated by 500 m) centered on the Kalantari Causeway.	March 6–April 20, 2018	
3	684 points along 12 paths with different lengths across the whole lake.	July 7–September 9, 2018	
4	1629 points along 12 paths of 10 km (separated by 500 m) centered on the Kalantari Causeway.	September 23–December 21, 2018	
5	8485 points along 24 paths with different lengths across the whole lake.	February 24–March 16, 2019	
6	11,019 points across the whole lake.	May 17–May 27, 2020	Darya Naghsheh Consulting Engineers

period, we used the closest image to that period window. As such, satellite images recorded on September 14, 2017, April 26, 2018, September 17, 2018, December 22, 2018, February 24, 2019, and May 17, 2020 were used for the first to sixth periods, respectively. We used the Ultra Blue (0.43–0.45 μm), Blue (0.45–0.51 μm), Green (0.53–0.59 μm), and Red (0.64–0.67 μm) bands of Landsat-8 for the analysis explained in Section 2.6.

2.4. Extraction of lake water body

To derive the bathymetric maps at multiple times as well as to update the lake level-area-volume relationship, we first needed to determine the water boundary of the lake at the time of satellite image being used. To this end, we used the k-means clustering, which is an unsupervised learning algorithm for a quick classification of an image into a desired number of feature classes (Likas et al., 2003).

The k-means clustering groups a dataset Ω, comprised of N vectors of v_i, $1 \le i \le$ N, into a k number of clusters defined by the user. Each vector, v_i, represents a pixel, and each element of v_i, $v_{i,\omega}$, $1 \le \omega \le$ M, carries a characteristic of the pixel. To cluster Ω, this method first chooses k arbitrary vectors, cl_c, $1 \le c \le$ k, as the centroids of the k clusters. Similar to v_i, each cl_c consists of M characteristics denoted as $cl_{c,\omega}$, $1 \le \omega \le$ M. Each pixel in Ω is then assigned to one of the k clusters based on the minimum Euclidean distance between the pixel's characteristics and the cluster centroids. The Euclidean distance (ED) between the vector v_i and the cluster centroid cl_c is computed as (Alfakih, 2018):

$$ED\left(v_i, cl_c\right) = \sqrt{\left(v_{i,1} - cl_{c,1}\right)^2 + \left(v_{i,2} - cl_{c,2}\right)^2 + \cdots + \left(v_{i,M} - cl_{c,M}\right)^2} \quad (1)$$

When the first clustering of all pixels is complete, the centroid of each cluster is updated and the iterative relocation is repeated until the centroid of each cluster is insignificantly different from its previous value.

Data from multiple bands or their combination such as Normalized Difference Water Index (NDWI), Modified Normalized Difference Water Index (MNDWI), Normalized Difference Vegetation Index (NDVI), Automated Water Extraction Index (AWEI), and Albedo (α) can be used as the training input to the classification algorithm. While former studies have demonstrated the high sensitivity of water body detection to the above indices (Feyisa et al., 2014; McFeeters, 1996; Xu, 2006), the accuracy is case-specific due to the impact of water constituents and substrate characteristics on the reflected energy from the water surface (Sun et al., 2017). As such, we tested different combinations of the above

indices with different numbers of k-means clusters to extract the water body that best describes the true water body boundaries using the surveyed lake boundary data.

Due to the presence of some natural or artificial features in the LU buffer zone such as artificial channels, the extracted water body identifies these features as water pixels, too. To exclude these features from the lake water body, we implemented a square-shaped sliding median filter of window size 11×11 on a given classified image. By moving the filter across the image, each pixel's value was replaced by the median value of its adjacent pixels. This process would assign a zero value to those water pixels that are dominantly surrounded by non-water pixels, thus confining the lake's true water body. Given the extracted water bodies from 1984 to 2020, the time series of LU surface area was computed based on the image pixel size, which was 30 m for the Landsat images used in this study.

2.5. Survey data on the lake boundary

To validate the approach adopted in Section 2.4 for delineating the LU water boundary, we conducted three field surveys on July 15 and July 17, 2019, in which the geographic location of 765 points along the lake water boundary was surveyed by the GARMIN eTrex Vista HCx handheld GPS device. The device positioning error is smaller than 10 m. The maximum error of this device is one-third of the Landsat's spatial resolution (i.e., 30 m); hence, the device accuracy was enough for tracing the LU water boundary. We chose the above survey timeframe (1) to minimize the lag-time between data collection and the pass of Landsat-8 satellite over the LU on July 18, 2019, and (2) to ensure a cloud-free condition based on the weather forecast. Fig. 2a–c depict the three surveyed paths mapped on a true-color image from Landsat-8 on July 18, 2019. We surveyed the 1.67 km path 1 (in red) and 1.41 km path 2 (in green) on the eastern shore of the LU from mid to north and south, respectively. Path 3 (in yellow) was surveyed by 1.63 km on the western shoreline towards the south.

2.6. Lake bathymetry derivation

In this section, we present the framework used for the derivation of bathymetric maps in the LU. The proposed methodology is not restricted to LU and can be employed in other environments of interest. In Section 2.6.1, we outline the procedure for pre-processing of the surveyed bathymetry data. In Section 2.6.2, we briefly describe the developed ANN model, which builds the relationship between water depth and water surface reflectance. Given a number of reflectance data at different bands from satellite imagery, the proposed approach for finding the optimum input band combination is described in Section 2.6.3. Finally, in Section 2.6.4 we further explain how different sets of hydrography data were clustered as the training data of the machine learning model to improve estimation accuracy.

2.6.1. Pre-processing of hydrography data

We performed a thorough pre-processing on the surveyed hydrography data to identify inappropriate data and exclude them from the training and testing dataset used in the machine learning model. We mainly considered two types of data as inappropriate data. First, given the water body extent from Section 2.4, there is a possibility that some surveyed points near the lake shoreline fall beyond the extracted water boundary. This can be due to (1) the error in the classification results at very shallow water depths, (2) the time gap between hydrography survey and satellite image acquisition, and (3) the error in recording the field data. In either cases, these points were identified and excluded from the rest of the analysis. Second, we examined the existence of any outliers in the remaining data. To this end, we used the concept of Mahalanobis distance and computed it for each observation in a given survey as:
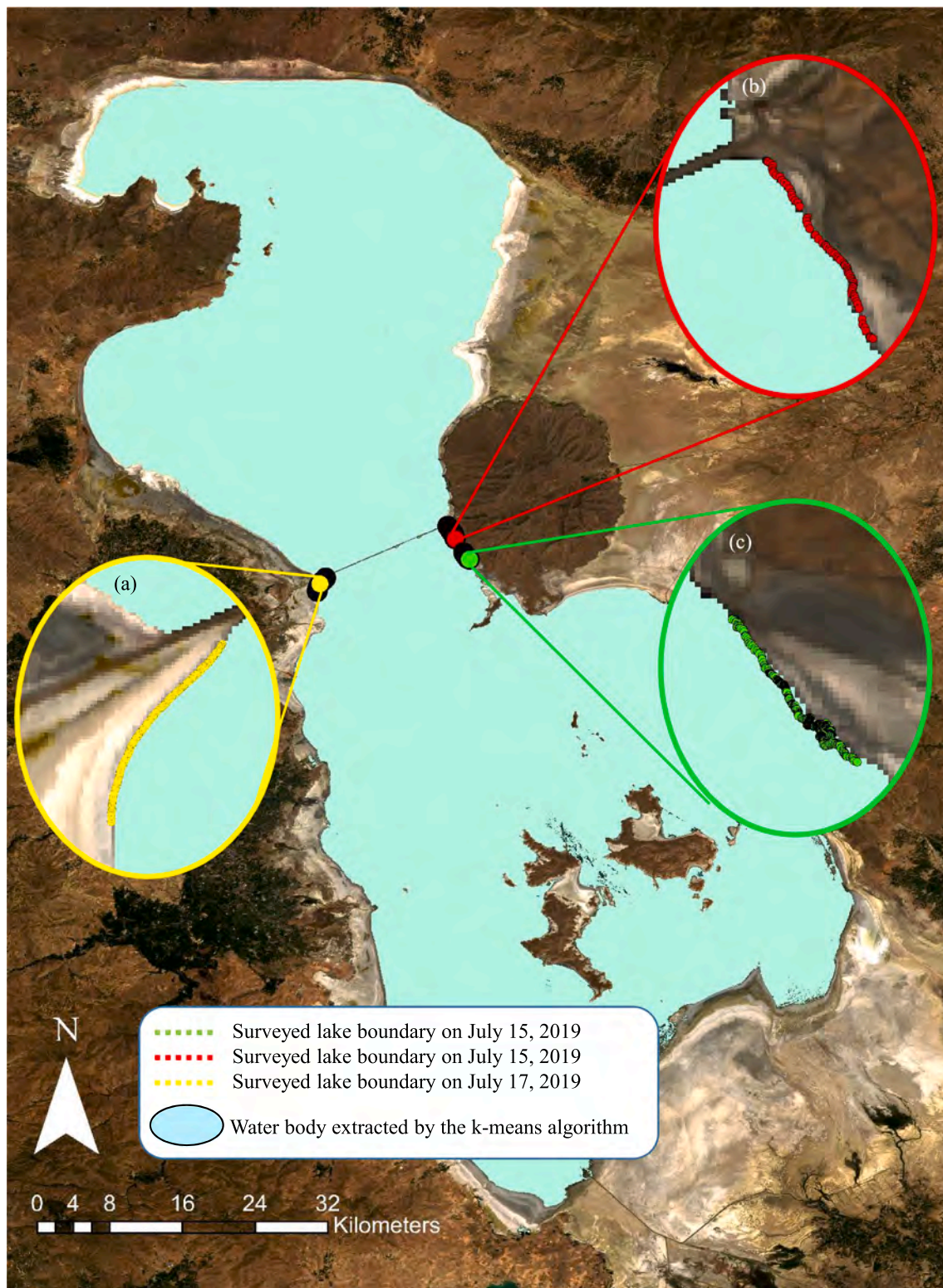
Fig. 2. Three surveyed paths along the Lake Urmia boundary on July 15 and July 17, 2019. The basemap shows the Landsat-8 RGB image on July 18, 2019. The lake water body extracted by the k-means algorithm is also shown in cyan. (For interpretation of the references to color in this figure legend, the reader is referred to the web version of this article.)

$$MD = \sqrt{(\mathbf{y} - \boldsymbol{\mu})^T S^{-1}(\mathbf{y} - \boldsymbol{\mu})} \qquad (2)$$

where MD denotes the Mahalanobis distance between the multivariate observation, $\mathbf{y}$, and its mean, $\boldsymbol{\mu}$, and S represents the covariance matrix of $\mathbf{y}$. For each data point, $\mathbf{y}$ includes the measured water depth as well as

reflectance values from the selected satellite bands. Since MD^2 has a Chi-Square distribution, we considered those data with p-value < 0.001 in the Chi-Square test as outlier and excluded them from the dataset. Several former studies have suggested this approach as a robust and reliable method for the detection of outliers in multivariate parameters

(e.g., Li and Jain, 2009).

2.6.2. Artificial neural network (ANN) model: architecture, training and testing

ANN is a supervised machine learning model that distributes data on inter-neuronal links to find the relationship between the model input and output (da Silva et al., 2017). A neural network architecture is composed of an input layer, hidden layer(s), and an output layer. Fig. 3 shows the structure of the ANN model developed in this study, which includes two hidden layers. Each layer of the neural network is made up of units called neurons. The neurons in the input layer, first hidden layer, second hidden layer, and the output layer are denoted by p ($1 \leq p \leq P$), m ($1 \leq m \leq M$), n ($1 \leq n \leq N$), and q ($1 \leq q \leq Q$), respectively, where P, M, N, and Q are the total number of neurons in the input layer, first hidden layer, second hidden layer, and the output layer, respectively. P equals to the number of input variables, which is the number of spectral bands in this study, and $q = 1$ for the network shown in Fig. 3.

The input variables to the neural network (i.e., reflectance values from different bands) are multiplied by certain relating weights and are then treated as the inputs of the neurons in the first hidden layer. This process can be expressed as

$$I_m^{h_1} = \sum_p W_{p \to m}^{h_1} B_l(\boldsymbol{X})_p + b_m \tag{3}$$

where $I_m^{h_1}$ is the input variable to neuron m in the first hidden layer h_1, $W_{p \to m}^{h_1}$ is the weight of the link that connects neuron p in the input layer to neuron m in the first hidden layer h_1, $B_l(\boldsymbol{X})_p$ is the reflectance value from band l ($1 \leq l \leq L$) at locations $\boldsymbol{X}\{x_g, 1 \leq g \leq G\}$ that enters neuron p, L equals to the total number of bands, x_g is the location of pixel g in a given satellite image, G is the total number of pixels in the image, and b_m is a constant value belonging to neuron m. Each neuron m in the first hidden layer applies a non-linear activation function to the input according to the following equation:

$$O_m^{h_1} = \frac{1}{1 + \exp(-I_m^{h_1})} \tag{4}$$

where $O_m^{h_1}$ is the output value of neuron m in the first hidden layer h_1. The above function, known as the Sigmoid function, is one of the most widely used activation functions in the context of multilayer perceptron

neural network (e.g., Choudhary et al., 2010). Although the activation function is a key parameter in a neural network functioning, if the developed ANN model is trained successfully with appropriate sufficient inputs, different activation functions are not expected to impose significant influence on the accuracy of the outcome (Feng and Lu, 2019).

Similar to the first hidden layer, the input to the second hidden layer, h_2, can be written as

$$I_n^{h_2} = \sum_m W_{m \to n}^{h_2} O_m^{h_1} + b_n \tag{5}$$

where $I_n^{h_2}$ is the input variable to neuron n in the second hidden layer h_2, $W_{m \to n}^{h_2}$ is the weight of the link that connects neuron m in the first hidden layer to neuron n in the second hidden layer h_2, and b_n is a constant value belonging to neuron n. Each neuron n in the second hidden layer applies the same activation function to its input, which ultimately gives

$$O_n^{h_2} = \frac{1}{1 + \exp(-I_n^{h_2})} \tag{6}$$

where O_n^2 is the output of neuron n in the second hidden layer h_2. Finally, the input of the output layer, which is indeed the output of the neural network, can be written as

$$D(\boldsymbol{X})^{pred} = \sum_n W_{n \to q}^{h_2} O_n^{h_2} + \varepsilon \tag{7}$$

where $D(\boldsymbol{X})^{pred}$ is the predicted water depth at locations $\boldsymbol{X}$, $W_{n \to q}^{h_2}$ is the weight of the link that connects neuron n in the second hidden layer to neuron q ($=1$) in the output layer, and ε is a constant value relating to the output layer's neuron.

From the above formulation, we observe that the developed ANN model contains six parameters, i.e., $W_{p \to m}^{h_1}$, $W_{m \to n}^{h_2}$, $W_{n \to q}^{h_2}$, b_m, b_n, and ε. These parameters were calibrated such that the following objective function is minimized:

$$\min \sum_{g=1}^{G} \left(D(x_g)^{pred} - D(x_g)^{obs} \right)^2 \tag{8}$$

where $D(x_g)^{obs}$ is the measured water depth at location x_g. We used the back-propagation algorithm to train the ANN model. This technique is a common approach for training an ANN structure. The main advantage of
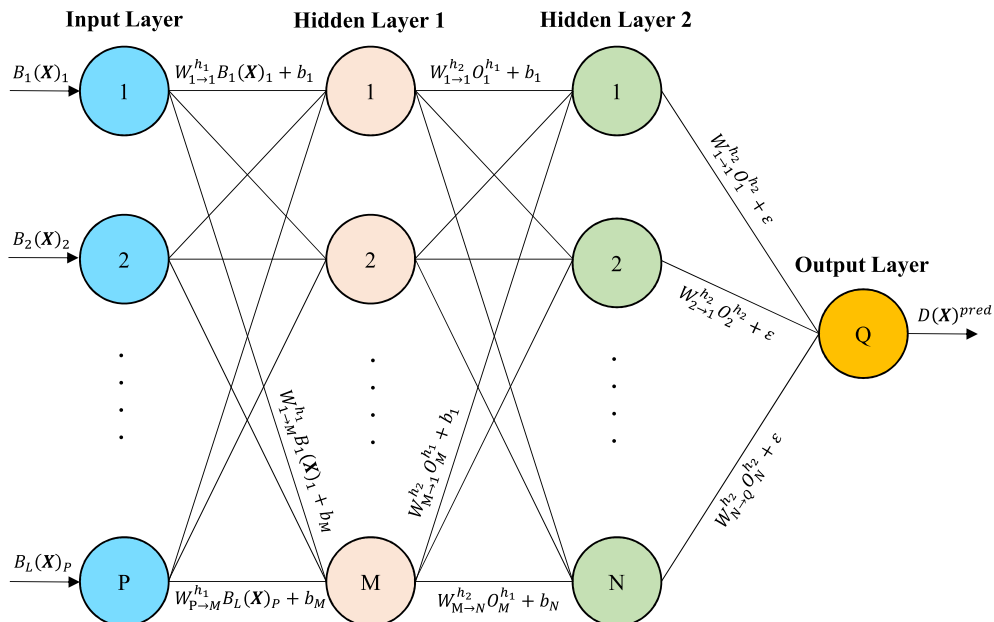

Fig. 3. The architecture of the developed ANN model to map water depth.

this scheme is the low computational cost for the training process and its reliable accuracy in most of the applications (Chauvin and Rumelhart, 1995). To determine the optimum structure of the ANN, we adopted the forward selection approach through a serious of Monte Carlo simulations (Han et al., 2011). To this end, we first considered one hidden layer and found the best number of neurons in the first layer by testing a relatively wide range of neurons. After setting the number of optimum neurons in the first layer, we added a new hidden layer and found the optimum number of neurons for the new layer by testing different number of neurons. The above process was repeated until adding a new layer with any number of neurons did not increase the prediction accuracy significantly.

In addition, we employed the *k*-fold cross-validation method with ten folds for the model training and testing purposes (Han et al., 2011). This method yields a more realistic model accuracy by using different parts of the training data, as compared to those approaches that select a random portion of data for training and the rest for model testing. To implement the *k*-fold cross-validation method, we first divided the training data into 10 seeds, where data from the nine seeds were used to train the model and data in the tenth seed were used to test the model. The training and testing processes were then repeated 10 times such that in each iteration, a unique combination of the nine seeds for training and one seed for testing were utilized. This guarantees the consideration of all non-repetitive combinations for model training and testing. After completing each process, the model accuracy for training and testing was recorded, separately. Finally, the average accuracy of 10 training and 10 testing processes was considered as the final accuracy of the model in the training and testing, respectively.

Here, we note that the uncertainty of prediction may be remarkable in the very shallow water depths near the lake water boundary or near the isolated land features within the lake body. To avoid the issue of masking the results, we filtered the model outputs based on the following criteria. Given the hydrography points surveyed in each period, we extracted the albedo of every point from Landsat-8 and plotted albedo against water depth. The relationship between these two quantities has a declining trend with more scattering in smaller water depths. For each period, we determined the water depth below which albedo showed a very narrow variation. Given these thresholds of water depth and albedo, we filtered those model outputs with water depth and albedo larger than their relating thresholds. This filtering ensures eliminating the wrong estimation of large water depths in very shallow areas.

2.6.3. Finding the optimum input band combination

The optimum input band combination is defined as the combination that gives the largest accuracy in estimating water depth using the developed ANN model. Various compositions of mainly ultra-blue (UB), blue, green, and red bands have been used in similar previous studies to extract bathymetric maps using optical sensors (e.g., Kabiri, 2017; Karimi and Bagheri, 2016; Knudby et al., 2016; Pacheco et al., 2015; Yunus et al., 2019). However, we performed a comprehensive analysis via a series of Monte Carlo simulations to take into account all possible band compositions as the input of the ANN model. To this end, we considered different combinations of the first seven bands of Landsat-8 as the alternative inputs to the model, which included 127 different inputs. For each set, the error of the ANN model in the testing process was calculated, and finally the band composition resulted in the least error was used as optimum input to derive the bathymetric maps.

2.6.4. Clustering the training dataset to improve water depth prediction

To improve water depth prediction, we clustered the hydrography data from all six surveys into three groups. The first group includes data of the first and third surveys at the end of summer and early autumn; the second group includes data of the second and sixth surveys in late winter and early spring; and the third group includes data of the fourth and fifth surveys in autumn and early winter. The basis of this clustering was the

similarity of atmospheric conditions as well as the angle of sunlight for each group, which diminishes the variation in the reflectance values. Table 2 shows the average air temperature (as a surrogate for the angle of sunlight), average pressure, and average relative humidity during the hydrography surveys. We observe that those periods aggregated into one category have a similar condition in terms of the above meteorological characteristics. We acknowledge that several other factors besides the angle of sunlight also influence the surface temperature. However, since the angle of sunlight is one determining factor of the energy reaching the earth's surface, the proximity of air temperature can be considered as the proximity of the angle of solar radiation in each data category.

3. Results

3.1. The accuracy of extracted water bodies

Having tested different numbers of clusters in the k-means algorithm, we found that three clusters yielded the most accurate results in delineating the lake water body. We also observed that the combined use of MNDWI and Albedo could successfully delineate the lake water boundary as contrasted against the three surveyed paths (see Fig. 2). The Euclidean distance between the extracted lake water boundary and the surveyed paths is 26 m, 17 m, and 4 m for paths 1 to 3, respectively, which is smaller than the image pixel size. Visual inspection of the extracted water body on July 18, 2019, against the relating RGB satellite image further confirms that the k-means algorithm could precisely extract the lake water body.

We note that the Euclidean distance from the k-mean clustering for path 3 is smaller than that for path 1 and path 2. We attribute such different accuracies to a few possible causes. First, the location of the lake water boundary is different between the time of field data collection and the satellite image acquisition. Indeed, there was a three-day gap between the time of surveyed water boundary along paths 1 and 2 (i.e., July 15, 2019) and the satellite passage (i.e., July 18, 2019), while it was only 1-day gap for path 3 which was surveyed on July 17, 2019. Regarding the lake fluctuation in H from 1271.69 m on July 15, 2019, to 1271.67 m on July 18, 2019, we expect a smaller difference between the observed and extracted water boundaries along path 3 as compared to the other two paths. We also noticed a windy condition on July 15, 2019, which further contributed to larger fluctuations along the lake shoreline on this day. Second, high soil moisture (near saturation) condition left by diurnal lake water recession can be another source of error. Third, the lakebed topography has a milder slope in the eastern than the western side of the lake. Therefore, a small rising or falling of the lake level can project into a larger progression or recession in the shore zone.

Here, we note that using NDWI thresholding, as a reduced complexity approach, is also very common for distinguishing water from non-water pixels. Nevertheless, since the LU water depth is very shallow near the boundaries and the salt deposits nearby the shoreline are almost saturated, it is expected that accurate delineation of the lake boundary from this approach would be challenging and might lead to unrealistic results. To examine this issue, we used the average NDWI of all pixels along the three surveyed paths as the threshold to extract the water body extent. We found that the extracted lake water body was significantly

Table 2
Average air temperature, average air pressure, and average relative humidity during the hydrography surveys.

Survey	Average Air Temperature (°C)	Average Air Pressure (HP)	Average Relative Humidity %
1	27.7	870.1	31.0
2	19.1	869.2	50.2
3	30.3	861.3	37.0
4	4.2	870.5	83.5
5	5.9	871.1	82.6
6	18.4	866.3	46.4

larger than reality, especially in the southwestern part of the lake. We further performed the same analysis at other multiple instances with different lake surface extent, which yielded the same conclusion. Therefore, using the same NDWI threshold for the extraction of water body at different times does not yield appropriate results, particularly in shallow environments. This highlights the necessity to tune the appropriate value of the NDWI threshold for each given image, which would be very time-consuming given the number of images to be processed in a long-term study period.

3.2. A threshold behavior in the lake Urmia level-area relationship

Fig. 4a shows the developed relationship between the LU surface area (A) and H, obtained from processing 172 satellite images (i.e., 75 images from Landsat 4–5 and 97 images from Landsat-8). We observe that two linear relationships with different slopes hold between A and H, which are expressed as

$$A = 2306.5H - 2930000, \quad H < 1271.31 \text{ m} \tag{9}$$

$$A = 351.65H - 443346, \quad H > 1271.31 \text{ m} \tag{10}$$

where A is in km^2 and H is in m above the mean sea level. Both relationships are statistically significant with the coefficient of determination (R^2) equal to 0.99. The two fitted lines intersect at H = 1271.31 m. The mean absolute error (MAE) of the first and second relationship is

55.46 and 48.82 km^2, respectively, which is equivalent to 3.21% and 1.07% of the average A below and above H = 1271.31 m, respectively. The root mean square error (RMSE) of A estimates from equations (9) and (10) is 73.64 and 69.45 km^2, which is equivalent to 3.57% and 1.45% of the average A below and above H = 1271.31 m, respectively.

Here, we observe that for H level less than 1271.31 m, A changes in a sharper rate with H, while this rate is milder for H larger than this threshold. This observation motivates the hypothesis that the east–west profiles of the lakebed are comprised of two trapezoids intersecting at the elevations close to 1271.31 m. Our preliminary investigations of some cross-sectional profiles computed from the hydrography data support this hypothesis. However, since the available hydrography data do not include complete profiles across the entire lake, we are far from making a general conclusion about this observation, and further exploration is left for future research.

Fig. 4b compares the results of the present study with the results obtained by the single fourth-order polynomial A-L relationship developed by Karimi and Bagheri (2016) as $H = (-4)^{-14}A^4 + 5^{-10}A^3 - 2^{-6}A^2 + 0.0042A + 1267$. We observe that the former relationship overestimates and underestimates A at H values smaller and larger than 1270.74 m, respectively, as compared to equations (9) and (10). As H increases, the difference between the results decreases until they become negligible near H = 1278 m. On average, the difference between the results of two studies is about 10.7%, which can be attributed to (i) the source of satellite images and (ii) the approaches
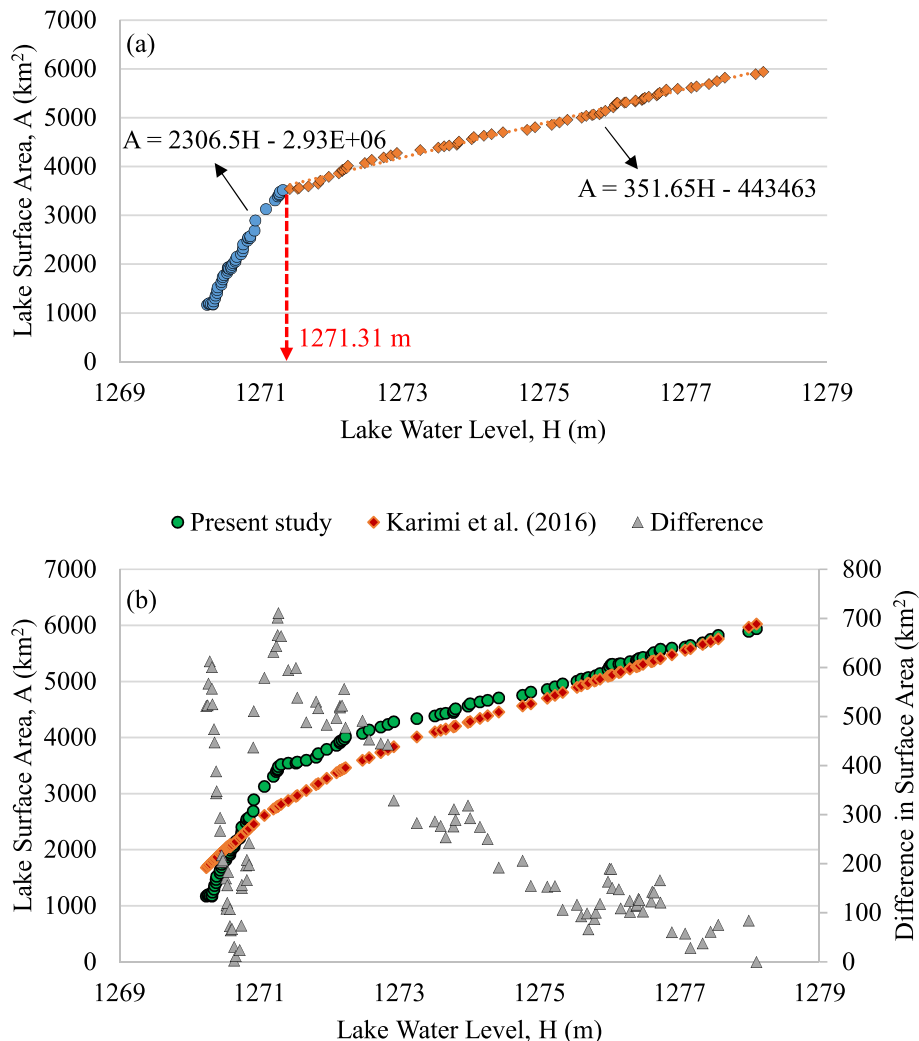

Fig. 4. Surface area versus water level relationship in the LU.

employed for the extraction of the lake water body. Utilization of Landsat imagery with a much finer spatial resolution in the present study as compared to AVHRR and MODIS imagery (with 1000 m and 500 m spatial resolution, respectively) used in Karimi and Bagheri (2016) resulted in a much improved delineation of the lake water body. In addition, the former relationship was obtained by examining 78 images from 1972 to 2014, while the present study used 172 images from 1984 to 2020 including data from those years when the lake surface was minimum due to the dramatic drying. Finally, unlike the former study, our extracted water body in the LU was validated against the field data, which adds confidence in the computed surface areas.

3.3. Spatial distribution of measured water depth

Having filtered the raw surveyed hydrography data, Table 3 gives the average, minimum, and maximum of the remaining measured water depth in each survey for the whole lake, northern half, and southern half, separately. We observe that after screening the raw data, there is still a sufficient set of data, i.e., 32,984 data points from all surveys, which could be effectively used to build the predictive model of water depth. It is also noteworthy that the average measured water depth in the sixth survey is remarkably larger than that in the other five surveys. We will investigate this observation in further details in Section 3.6.

3.4. The ANN model accuracy for estimating water depth

Table 4 presents the ANN model accuracy for some selected input band combinations that yielded the most accurate results by using the first group of processed hydrography data (described in Section 2.6.4) as the training data. We observe that the combination of UB, blue, green, and red bands resulted in the highest accuracy in estimating the water depth (MAE = 3.6 cm). The results (not shown here) obtained by using the second and third group of hydrography data yielded the same conclusion. Table 4 also reveals that if only one band is used as the model input, the green band gives the highest accuracy (MAE = 9.1 cm). This can be attributed to the LU greenish color in most months, which results in a high reflection of electromagnetic waves in this band as compared to the other visible bands. In the case of selecting two bands as the model input, the blue and green bands (as compared to other two-band combinations) give the most accurate results in expressing the LU water depth changes (MAE = 7.6 cm). Finally, three-band combination of UB, blue and green gives the least MAE equal to 6.6 cm.

A couple of points are worth mentioning here. First, increasing the number of selected bands does not necessarily lead to enhanced accuracy of water depth estimation. For instance, selection of all Landsat-8 satellite bands (non-thermal bands) provided less accuracy than the selection of the first four bands. Also, selection of the green band alone provided higher accuracy than the selection of the main two-band combinations. Second, in many previous studies (e.g., Kabiri, 2017; Pacheco et al., 2015; Yunus et al., 2019) the blue band has been proposed in combination with other bands to estimate water depth, while we found the green band more effective in our study area. This indicates that in the RS of aquatic environments, there is no optimal band-combination that necessarily applies to all water bodies. The presence

Table 4
The ANN model accuracy for some selected input band combinations.

Number of Selected Bands	Selected Band(s)	MAE (cm)	Number of Selected Bands	Selected Bands	MAE (cm)
1	UB	12.5	2	B + G	7.6
1	B	13.3	2	B + R	17.7
1	G	9.1	2	G + R	30.5
1	R	12.8	3	UB + B + G	6.6
2	UB + B	10.3	3	B + G + R	7.7
2	UB + G	16.5	4	UB + B + G + R	3.6
2	UB + R	9.4	7	All Bands	5.1

of different solutes or suspended substances plays an important role in differentiating the optimal properties of water from one aquatic system to another.

Using the band-combination of UB, blue, green, and red as the input of the ANN model, the final three models were built for the three groups of hydrography data, separately. Table 5 gives the accuracy of the models in the training and testing processes. We observe that the highest accuracy was obtained from the first group of data that were collected at the end of summer and the beginning of autumn. The MAE of the testing process for the first, second, and third groups of data is 3.3 cm, 9.7 cm, and 12.1 cm, respectively. The RMSE in the same process for the first, second, and third groups of data is 7.7 cm, 15.6 cm, and 17.9 cm, respectively. All statistical measures confirm the high accuracy of the developed models.

The in-situ data clustering approach used in this study witnessed the high accuracy of water depth prediction. Alternatively, other approaches could also be employed to use the hydrography data for training and testing the prediction model. For instance, we could use the data collected in each period to train the ANN model for that period and generate the relating bathymetric map. This approach suffers a couple of drawbacks. First, at some data collection periods, i.e., the first, second, and fourth surveys, the collected data were concentrated around the causeway. Regarding the LU's approximate length of 130 km (in April 2019) and its large area, it is expected that the variability of lakebed topography and chemical properties of the lake water induce considerable impact on the spectral properties of the lake water from north to south. Therefore, the spectral behavior of the lake around the causeway cannot be attributed to the whole lake. Indeed, when a neural network

Table 5
Accuracy assessment of the developed ANN models for the three groups of hydrography data.

Data Group	Process	MAE (cm)	RMSE (cm)	R^2
1	Training	3.3	7.7	0.9
	Testing	3.6	7.8	0.9
2	Training	9.4	14.8	0.9
	Testing	9.7	15.6	0.9
3	Training	11.8	17.7	0.8
	Testing	12.1	17.9	0.8

Table 3
Statistics of measured water depth in each survey for the whole lake, northern half, and southern half.

Survey Stage	Survey Period	Average Measured Water Depth (m)			Minimum Measured Water Depth (m)			Maximum Measured Water Depth (m)		
		Whole Lake	North	South	Whole Lake	North	South	Whole Lake	North	South
1	Sep. 23–Oct. 22, 2017	0.97	0.79	1.06	0.00	0.00	0.00	2.36	2.27	2.36
2	Mar. 6–Apr. 20, 2018	0.87	0.79	0.92	0.00	0.00	0.00	2.51	2.51	2.49
3	July 7–Sep. 9, 2018	0.47	0.22	0.57	0.00	0.00	0.08	1.45	0.55	1.45
4	Sep. 23–Dec. 21, 2018	0.56	0.51	0.60	0.00	0.00	0.00	2.61	2.57	2.61
5	Feb. 24–Mar. 16, 2019	0.88	0.64	1.10	0.00	0.00	0.00	2.41	2.41	2.20
6	May 17–May 27, 2020	2.26	2.36	2.16	1.17	1.20	1.17	3.36	3.13	3.36

model is trained using any of the data from the first, second, and fourth surveys, the output of the model learns the relationship between spectral behavior and water depth in only the same period. Consequently, by applying each trained model to extract water depth (or bathymetric) maps in the whole lake, we cannot expect appropriate estimations in other places than near the causeway. The second drawback of this approach is that the depth data collected in some survey periods may only cover a certain range of depths. For instance, the minimum depth measured in the sixth survey was 118 cm; hence, it can be expected that a model developed solely using data from the sixth survey cannot estimate the shallow depths, especially near the lake shoreline. Considering the above issues, it can be concluded that the approach of using data from each period to extract the water depth map of the same period is not suitable and cannot properly describe the whole lake condition. The
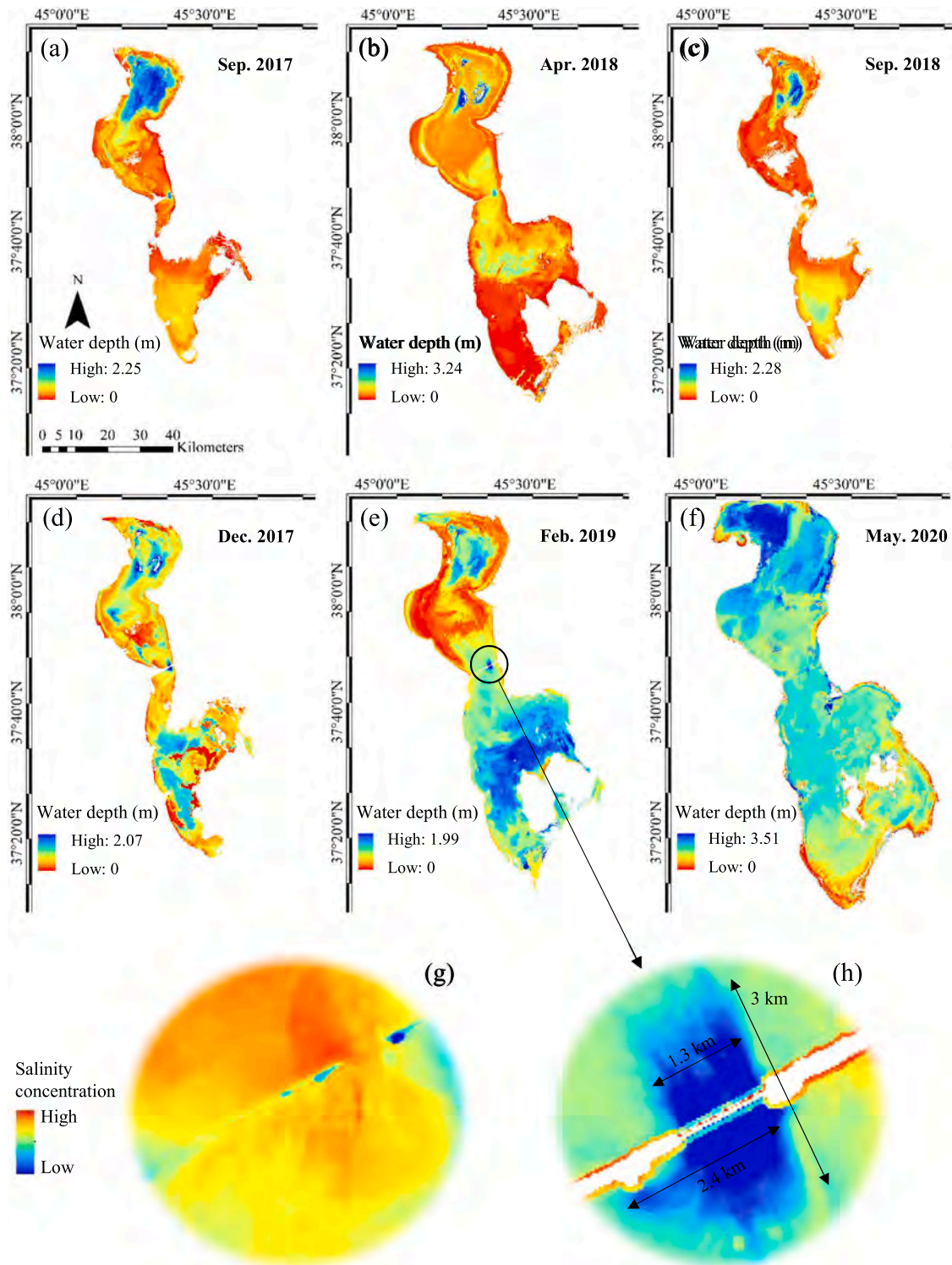

Fig. 5. Spatial distribution of water depth in Lake Urmia. Panels (a–f) illustrate the estimated water depth from the ANN model on September 14, 2017, April 26, 2018, September 17, 2018, December 22, 2018, February 24, 2019, and May 17, 2020, respectively. Panel (g) indicates the spatial variation of salinity near the bridge (image modified from Fig. 7 in Bayati and Danesh-Yazdi (2021)). Panel (h) shows the extent of local scouring in the vicinity of the bridge.

second possible approach was to combine data from all six surveys and develop a single model to generate bathymetric maps for each period. This approach has also limitations because, at different times of a year, spectral patterns change in a water body. Indeed, since the angle and intensity of the sun's illumination change over time, different radiations can be received by the satellite sensor for the same water depth. In addition, changes in the air humidity and the constituent particles of the atmosphere in different seasons of a year further influence the amount of reflection received by satellite. Therefore, using the second approach to build a single model for the whole year can also impose remarkable errors in deriving the bathymetric maps.

3.5. Dynamics of water depth change in Lake Urmia

Fig. 5 illustrates the spatial distribution of estimated water depth in the LU on September 14, 2017, April 26, 2018, September 17, 2018, December 22, 2018, February 24, 2019, and May 17, 2020. Table 6 further gives the average and the coefficient of variation (CV) of water depth in the whole lake, the northern half, and southern half, separately. Comparing the lake maps between the third and sixth stages (as the driest and wettest stages in the study period, respectively) indicates a considerable increase in the lake surface area in 2020 when the two islands in the south were surrounded by the lake water. The results indicate that the average water depth in the LU was 0.62 m, 0.57 m, 0.43 m, 0.53 m, 0.86 m, and 2.00 m in the survey stages one to six, respectively. H at the relating periods was 1270.32 m, 1270.75 m, 1270.27 m, 1270.54 m, 1270.82 m, and 1271.91 m, respectively. This indicates that in general, the average water depth in the lake increases with the increase in H. The exception to this observation is the change of water depth in between surveys one and two when the lake level increased by 0.43 m while the average lake water depth changed very slightly. According to Table 6, the average water depth in the south half was increased during this period, while the opposite took place in the north half. Together with the decreased CV of water depth in the whole lake, it seems that the lakebed topography became uniform during this period, which is also evident in Fig. 5b.

We also observe that the average water depth in the northern half is larger than that in the southern half in the survey periods one, two, and six, while the reserve holds in the survey periods three and five. In the fourth period, there is a negligible difference between the average water depths in the two halves, which implies that the variability of water depth across the whole lake has a similar pattern. This is confirmed by the CV of water depth, which is almost the same in the north and south halves and thus the whole lake. We further note that the CV of water depth (with respect to the whole lake) changed from 0.80 in the first survey period to 0.32 in the sixth survey period. Such a considerable decrease in CV is concurrent with the increase of 1.59 m in H, which implies that by increasing the volume of inflow to the lake, the spatial variability of water depth decreases. Indeed, in the sixth period when the lake recorded the highest level since 2010, there is a slight difference between the CV of water depth across the lake, i.e., 0.28 for the northern half and 0.32 for the southern half. In contrast, in the first period when the lake experienced one of its historically lowest levels, the CV of water depth is considerably different between the northern and southern

halves as evidenced by 0.77 against 0.47, respectively. This is mainly because of the diminished flow exchange between the two halves in this period, which was due to the significant reduction in the lake inflow from the southern feeding rivers.

The impact of increased flow velocity on the lakebed local scouring in the vicinity of the Kalantari Bridge is also clear in all water depth maps. Fig. 5h indicates a zoomed-in image of the lake water depth at the location of the bridge where water exchange between the northern and southern halves takes place. It is seen that the extent of the local scoured area in the south-north direction is about 3 km, while the width of the scour is about 1.3 km and 2.4 km in the northern and southern sides of the bridge, respectively. We explored the scour region in all the other maps and found similar observations. Given the counter-clockwise direction of flow in the LU (Safavi et al., 2020), we observe that the return flow from north to south could scour the lakebed in the transverse direction to a larger extent than that caused by the south-north flow.

In Fig. 5g, we further show the spatial variability of salinity concentration around the bridge in March 2019 (Bayati and Danesh-Yazdi, 2021) as a cross-reference for the lake dynamics in this region. It is obviously seen how the saltier water from the north concentrates the lake water in the scoured zone. We note that the spatial scale of the zone shown in Fig. 5g is larger than that in Fig. 5h due to the other processes that influence salt dispersion.

Given the water depth maps, we can derive the bathymetric maps by subtracting each map from the relating lake water elevation. We refused to report the derived bathymetric maps, as their spatial variation is the same as that for the water depth maps. However, we discuss how they can be used to study the dynamics of salt precipitation and dissolution in Section 4.3.

3.6. Water level vs. stored volume in Lake Urmia

Fig. 6 shows H versus stored water volume in the LU between 2017 and 2020. The six color-points on this plot relate to the volumes that were estimated from the bathymetric maps derived in Section 3.5. The dotted blue curve shows the predictive relationship between the H and volume as proposed by the former and only relevant study in the LU (Water Research Institute, 2015), which was derived for the lake's very dry condition. We estimated the lake volume in surveys one to six as 0.77 BCM, 1.27 BCM, 0.45 BCM, 0.79 BCM, 1.96 BCM, and 7.0 BCM, respectively, while the predictive relationship gives 1.14 BCM, 2.01 BCM, 1.23 BCM, 1.56 BCM, 2.18 BCM, and 5.25 BCM, respectively. Both results witness that the lake volume during survey six (May 2020) was significantly larger than that in survey five (February 2019). This is because of the lake restoration with the aid of a large inflow from the feeding rivers in this period. The inset of Fig. 6 further shows the time series of H in LU between 2017 and 2020, which indicates that H increased by 1.09 from February 24, 2019, to May 17, 2020.

The absolute difference between our results and the former predictive relationship in surveys one to six is 0.37 BCM (32.3%), 0.74 BCM (36.6%), 0.78 BCM (63.2%), 0.77 BCM (49.4%), 0.23 BCM (10.3%), and 1.7 BCM (33.4%), respectively. With respect to the water volume magnitudes estimated from the bathymetric maps, the former predictive relationship overestimates the lake volume in survey periods one to five,

Table 6
Statistics of the estimated water depth in Lake Urmia. The statistics are presented for the whole lake, the northern half, and the southern and half, separately.

| Survey Stage	Date of Satellite Imagery	Lake Level (m)	Average Water Depth (m)			Coefficient of Variation of Water Depth		
			Whole Lake	North	South	Whole Lake	North	South
1	Sep. 14, 2017	1270.32	0.62	0.76	0.42	0.80	0.77	0.47
2	Apr. 26, 2018	1270.75	0.56	0.65	0.49	0.69	0.60	0.74
3	Sep. 17, 2018	1270.27	0.43	0.38	0.47	0.72	0.94	0.46
4	Dec. 22, 2018	1270.54	0.54	0.54	0.53	0.48	0.47	0.50
5	Feb. 24, 2019	1270.82	0.86	0.55	1.11	0.47	0.59	0.24
6	May 17, 2020	1271.91	2.00	2.28	1.80	0.32	0.28	0.31
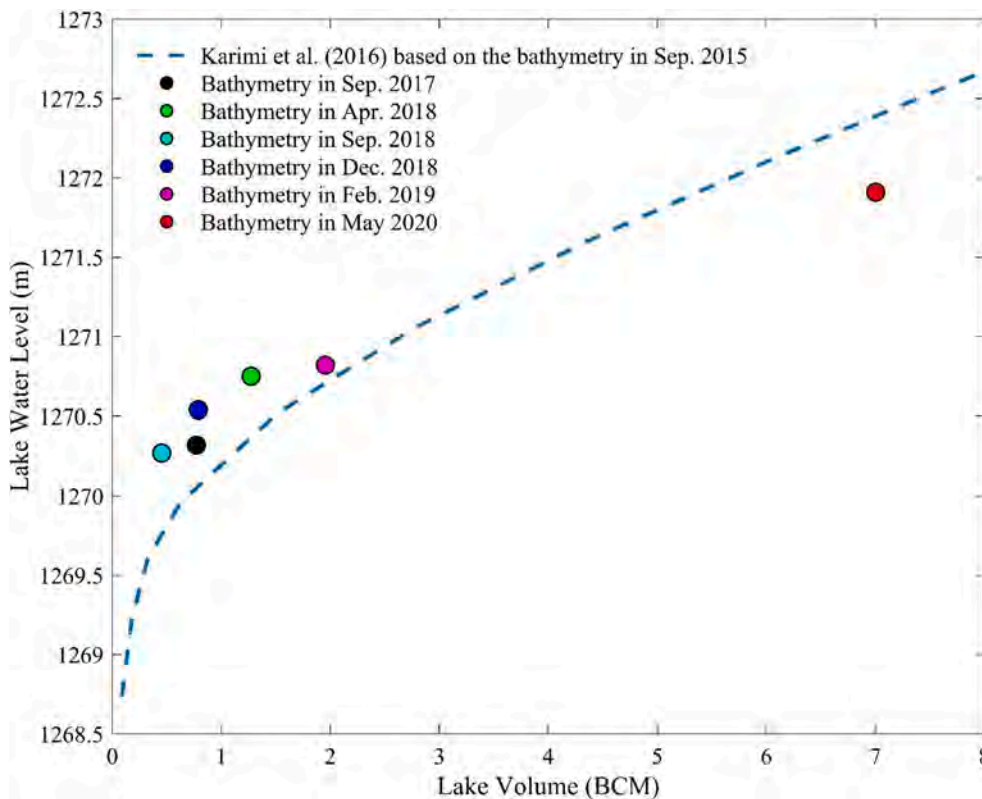
Fig. 6. Water level versus stored water volume in Lake Urmia. The dotted blue curve shows the proposed predictive relationship between the lake level and volume based on the bathymetric map derived in September 2015 (taken from the study of Karimi and Bagheri (2016)). Color dots show the lake volume estimated from the bathymetric maps derived in the present study between 2017 and 2020. (For interpretation of the references to color in this figure legend, the reader is referred to the web version of this article.)

while it largely underestimates the lake volume in survey period six. In particular, our results indicate that in May 2020, LU had 1.7 BCM of water more than what is believed based on the former predictive relationship. This is an important observation as it can be used to assess the degree of lake restoration, regardless of the source of water provided by storm rainfalls or basin management practices.

4. Discussion

4.1. Revisiting the level-area-volume relationship in Lake Urmia

Currently, ULRP uses the former predictive A-H and V-H relationships developed by Karimi and Bagheri (2016) to estimate the lake area and lake volume at a desired time, given the H measured at a ground station. We demonstrated that the difference between the formerly developed A-L relationship and that obtained in the present study, i.e., equations (9) and (10), is not significant. Nevertheless, we showed that there is a remarkable difference between the predicted volumes from the formerly developed relationship and our estimates based on the intensive hydrography data surveyed between 2017 and 2020.

We argue that the reason for such a notable difference arises from some major issues in the study of Karimi and Bagheri (2016). First, they developed a multi-linear regression model to construct the relationship between the measured water depth and multi-spectral reflectance data. However, the employed multi-linear regression model cannot adequately capture the complexity in the relationship between water depth and reflectance. The superiority of intelligent learning models over the traditional approaches like linear regression has been already demonstrated by former studies (e.g., Liu et al., 2018; Mohamed et al., 2016; Sagawa et al., 2019). Second, the measured hydrography data to calibrate the multi-linear regression model included 640 points that all were surveyed only in the north half of the LU. Regarding the large variability of the bed topography as well as water depth across the LU surface area, those measurements could not appropriately describe the whole lake condition and were merely representative of the bathymetric

changes in the north half. Third, they used a single bathymetric map of the LU derived in 2015 to estimate the lake volume at other times. To map the topography of dried areas beyond the lake water body, they first classified Landsat images to determine the edge of the water body at different elevations. Then, they fitted a digital elevation model to the distance between these edges and the playa edge along the Golmankhaneh station as a reference point (Karimi and Bagheri, 2016; Water Research Institute, 2015). This process clearly imposes large uncertainty in the estimated volumes, as it does not take into account the impact of lakebed fluctuations due to salt precipitation and dissolution on the estimated lake volume at other times than September 2015.

According to our results in Fig. 5 and Table 6, the bed elevation in the LU is highly dynamic in time; hence, an appropriate prediction of the lake volume at a given time must be conducted by using the bathymetric map of the same time. Therefore, the level-volume relationship developed in 2015 to predict the lake volume in a range of H's between 1267 m and 1278 m ignores any changes in the lakebed elevation imposed by salt precipitation and dissolution. As such, we conclude that no single level-volume relationship can be proposed for the LU or any other saline lake to represent the lake condition over time. This is further demonstrated in Fig. 7 where for each of the bathymetric maps derived in Section 3.5, we extracted the relating level-volume relationship. The maximum H for each curve is the maximum bed elevation in the relating bathymetric map. The wide range of relationships in this plot clearly reflects the influence of the lakebed fluctuations due to salt precipitation and dissolution on the level-volume relationship.

We note that Sima and Tajrishy (2013) also attempted to derive the level-volume relationship in the LU by (i) integrating the level-area relationship within the range of lake altimetry data, and (ii) calibrating a couple of analytical models for the lake geometry, i.e., Nilsson's power-function model (Nilsson et al., 2008) and simple truncated pyramid model. Assuming the integration approach gives the most accurate results as compared to the other two models, the applicability of the derived fourth-order polynomial relationship is still limited. This is because the estimation of the lake volume at a given H requires the
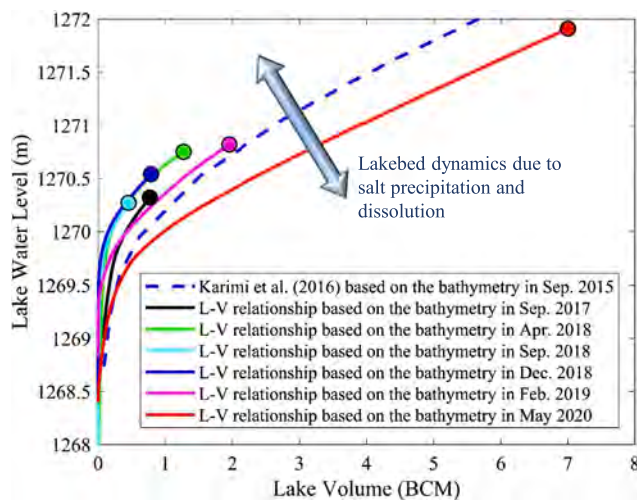
Fig. 7. The impact of lakebed dynamics on level-volume relationship in Lake Urmia. Each curve shows a hypothetical level-volume relationship for the Lake Urmia if a given bathymetric map is used to compute the lake volume at different water levels.

knowledge of the lake volume at a reference H, used as the minimum bound of the integration. The so-called reference volume can be only determined from in-situ hydrography data, and it also changes in time, i. e., different reference volumes can be observed at the same H. Therefore, the proposed level-volume relationship cannot express the lake geometry changes in time and may yield large errors within a certain range of H.

The above pieces of evidence underline the necessity of timely hydrography data collection in the LU to monitor the lake dynamics and to estimate the lake volume, appropriately. An accurate bathymetry also helps study other physical processes taking place in the LU. One of the poorly understood issues in the study area has been the lake saltwater exchange with the surrounding aquifer. Using limited hydrochemistry and isotopic field data, Amiri et al. (2016a, 2016b, 2016c) found that the sediment deposits on the lakebed act as a barrier, preventing the chemical interaction between the lake and groundwater and thus minimizing the saltwater intrusion from the lake (see also Mehr et al. (2019) for similar conclusions). However, a few other studies (Tourian et al., 2015; Vaheddoost et al., 2015; Vaheddoost and Aksoy, 2018) reported a significant correlation between the lake water fluctuation and groundwater level by analyzing sparse groundwater data recorded by observation wells in the region. Javadzadeh et al. (2020) further conducted a comprehensive analysis on the cross-correlation between the lake and groundwater level using data recorded from 797 observation wells in 17 adjacent aquifers between 2001 and 2018. They also found a significant correlation between these two quantities, where the direction of correlation changes spatially depending on whether the lake is losing or gaining. Regarding the statistical nature of the above studies, Sheibani et al. (2020) have extended this exploration through a series of numerical simulations considering the impacts on saltwater intrusion by the lakebed sediment layer thickness, lakebed sediment hydraulic conductivity, and aquifer hydraulic conductivity. However, they set up the geometry of their numerical model based on the sparse hydrography data (ISRC, 2018), but not the bathymetric map of the whole lake due to its unavailability. It is seen that the lack of updated information about the dynamics of bathymetry in the LU has been a missing component for this and other relevant studies in the region (e.g., Abbaspour et al., 2012; Arabsahebi et al., 2020; Saemian et al., 2020; Safavi et al., 2020; Sharifi et al., 2018). Therefore, the results of the present study can be leveraged by future researches for analysis and synthesis purposes, as it provides the most comprehensive information on the LU bathymetric changes over a long period.

4.2. The interplay between the quality of field data and remotely sensed imagery in controlling the accuracy of water depth prediction

The results of the ANN model accuracy indicated that the prediction accuracy of water depth for the first data group was better than that for the second group, followed by accuracy for the third group. This observation was not expected regarding the impressive size of hydrography data in the third group and its spatially uniform distribution. We investigated the reason(s) for this finding by exploring the possible impact of atmospheric condition on the quality of data retrieved from satellite images. The average relative humidity and air temperature in the period corresponding to the first group of data were 34% and 29 °C, respectively. These measures were 48.5% and 18.8 °C for the second group of data, respectively, and were 83.1% and 5.1 °C for the third dataset, respectively. It is interesting to observe that the model error is positively and negatively proportional to relative humidity and air temperature, respectively. Indeed, under the higher relative humidity, the absorption and diffusion of electromagnetic waves by the water particles in the air reduce the useful information received by a satellite sensor from the ground. Despite using atmospherically corrected images, we note that the advantage of high-quality training data obtained from the field measurements could not overcome the impact of remaining noise in the satellite data on the accuracy of water depth estimation.

We also note that even though Manaffar et al. (2020) assessed the turbidity of LU and concluded the governance of relatively low turbidity in the majority of the LU surface area, we cannot extend this conclusion to the results of this study due to the lack of relevant data in our study period. Nevertheless, the order of estimation accuracy obtained in this study is much smaller than that expected in turbid water cases, which highlights the acceptable validity of our results.

4.3. Dynamics of salt dissolution and precipitation in the Lake Urmia

Changes in the lakebed elevation are expected to happen due to salt dissolution or precipitation, considering the hyper-salinity of the LU. Intuitively, it is expected that salt dissolution and precipitation take place by the lake wetting and drying, respectively. However, the state of lake replenishment versus depletion is not the only factor in determining whether salt dissolution or precipitation dominates in the lake. This is because, under a similar change of water volume, salt precipitation can take place in both cases of lake recession and progression. In the former case, the loss of water increases the salt concertation in the lake, which can precipitate if the saturation degree is reached. In the latter case, the salt concentration of the progressive water also increases as it dissolves the lakebed salts that were deposited during the former lake recessions. Therefore, the direction of change in the lake water volume cannot solely describe the relative degree of salt precipitation and dissolution. Instead, we suggest that the interplay between (i) the volume of freshwater flow into the lake and (ii) the extent of lakebed inundation or drying area determines the degree of salt precipitation or dissolution in the lake. The relative influence of the above two quantities can be expressed as the ration $\Delta V/\Delta A$, where ΔV and ΔA is the change in the lake volume and surface area in a given period, respectively. Larger $\Delta V/\Delta A$ indicates that a variation in the water volume projects into a larger change of the lake level than the surface area. The state of salt precipitation and dissolution is determined by the sign of ΔV (or ΔA), that is, positive and negative ΔV (or ΔA) indicates dissolution and precipitation, respectively.

If the lake receives a significant freshwater inflow that increases the lake volume at a greater rate than the lake surface area, dissolution dominates due to a couple of major reasons. First, the impact of freshwater in diluting the lake water dominates the rate of concentration by dissolving lakebed salts. Second, the inflow can circulate faster throughout the lake, which facilitates salt dissolution across a large extent of the lake. The reverse condition, i.e., salt precipitation, can

occur under the same magnitude of $\Delta V/\Delta A$, but with opposite sign and at different absolute magnitudes of ΔV and ΔA. This situation holds during the lake recession when the loss rate of water volume is much larger than the lake area shrinkage. We note that in general, $\Delta V/\Delta A$ cannot be accounted as a surrogate for the change in the average water depth. Depending on the geometry of the lake bathymetry and the state of H, $\Delta V/\Delta A$ may take a large value, but the change in the average water depth remains mild.

Given the above context, we hypothesize that a negative correlation holds between the salt precipitation rate and $\Delta V/\Delta A$, i.e., by shifting from smaller to larger $\Delta V/\Delta A$ magnitudes between two consecutive periods, the lake condition is switched from precipitation to dissolution. According to Fig. 6, since LU has experienced multiple wetting and drying episodes during the study period, we could examine the above hypothesis by studying the amount of salt precipitation and dissolution given the changes in the lake surface area, stored water volume, and bathymetry. Nevertheless, we could not conduct this analysis due to the lack of elevation data on the terrestrial portion of the LU. Indeed, the extent of the derived bathymetric maps was confined to the boundary of the lake water body, which changes from one time to another. As such, if the objective is to compute the amount of salt precipitation and dissolution from, e.g., stage one to stage two (see Fig. 5), we need to know the bed elevation in the region beyond the overlapping area between the bathymetric maps of the aforementioned stages. Therefore, the difference between two consecutive bathymetric maps only provides information about the lakebed changes within the overlapped surface area of the maps and thus misses any information about the lakebed changes in the nearby areas. This limitation poses a quest to plan for a comprehensive and timely data compilation on the lakebed elevation with the aid of both field data and RS.

4.4. Limitations and caveats

Despite the advantages of the employed modeling framework, this study carries some challenges and limitations. As Table 1 shows, some hydrography surveys were conducted over a long period, while limited satellite images (i.e., one or two) were available during the relating period. For further research, we suggest using data from other satellites such as Sentinel-2 to receive more images at a finer temporal resolution, especially during the high lake-inflow seasons when the lakebed is remarkably dynamic. Furthermore, we had to use a single H value for the whole period of each survey. This was particularly evident in the third and fourth survey periods when the change in H was considerable. Therefore, the water surface elevation at the time of satellite image acquisition could be different from that at the time of hydrography data collection. Unfortunately, we could not resolve this issue because the hydrography data provided from ULRP did not include daily information on the collected data over these periods.

The other challenge of this work was rooted in using a single value of H for the whole lake in a given day. As described in Section 2.2, ground measurement of H is available only from one station in the lake, which does not describe diurnal fluctuation in H across the whole lake. The difference in H between the northern and southern halves becomes distinct during the lake dryer conditions when the segregation of the two halves occurs at low water surface elevations. Under these circumstances, the water surface elevation in the two halves cannot be considered the same as that measured at the Golmankhaneh station. The use of single lake water elevation is further projected into the computation of bathymetric maps as well as the lake level-volume and level-area relationships.

Finally, we acknowledge that the surveyed hydrography data at some periods did not have a uniform spatial distribution across the lake. Given the fact that physical characteristics of water and substrate impose a remarkable influence on the relationship between water depth and surface reflectance, sufficient and uniformly distributed hydrography data is necessary for an appropriate estimation of water depth across

the whole lake. We attempted to tackle this issue by clustering data from all survey periods into specific groups, which greatly improved the predictive model performance. The clustering operation further facilitated model training over the whole spectrum of the lake water depth at a time of interest. However, the above consideration should be taken into account in future data collection in the LU to smoothen the process of water depth modeling and to provide hydrography data that include the smallest to largest possible water depths to measure. Also, since the spatial variability in the lake water chemistry influences the spectral properties of pixels with the same water depth, the hydrography data collection can be better guided by classifying the lake water based on a given water quality measure to ensure that data collection takes place at all classes with distinct quality characteristics.

4.5. Final remarks

Using RS data in water bodies is challenging mainly due to: (i) the high amount of electromagnetic absorption, which masks the information carried by water physicochemical characteristics, (ii) the impact of turbidity on water-leaving reflectance, (iii) the contrasting accuracy of many atmospheric correction methods developed for the calculation of surface reflectance. While the above challenges are related to all water bodies, RS of shallow water environments is further subjected to the radiometric interaction of water and substrate. Nevertheless, a few points are worth mentioning here. First, the Signal to Noise Ratio (SNR) is supposed to be higher in bright and shallow waters due to the lower electromagnetic absorption as compared to that in deep waters (Kutser et al., 2020). Second, given the substrate influence on water-leaving reflectance particularly near shorelines, this impact over a range of similar water depths would be uniformly distributed in water bodies with a uniform bed composition (such as the LU with salty bed). This would in turn diminish water depth estimation bias from machine learning algorithms that are capable of deciphering non-linear relations between water depth and surface reflectance if sufficient well-distributed in-situ data are employed. Third, the literature witnesses that RS of turbid waters has been less successful as compared to that in non-turbid waters because high turbidity could strongly mask the spectral information of water (Matsushita et al., 2008; Oyama et al., 2007). In turbid waters (also known as Case-II waters) containing high amounts of Optically Active Substances (OAS), e.g., suspended solids, phytoplankton, and colored dissolved organic matters, high absorption of the electromagnetic spectrum by OAS reduces the decipherable information from the water spectral signature. Also, due to the complex optical interactions between OAS components, we may not be able to derive a unique spectral pattern for a variable of interest (e.g., water depth) across a whole water body (Shen et al., 2010). As such, the significance of a careful selection of suitable atmospheric correction method is more critical in turbid waters as compared to that in non-turbid waters (Caballero and Stumpf, 2020; Wei et al., 2018). In such cases, the atmospheric correction schemes specifically developed for water environments, e.g., SeaDAS and ACOLITE, are recommended (Ilori et al., 2019; Vanhellemont, 2019; Vanhellemont and Ruddick, 2014). Regarding the above challenges and opportunities, it is concluded that the proposed framework in this study can be employed effectively to extract the bathymetric map of a water body of interest. To this end, the availability of proper information on the physicochemical characteristics of the water body is necessary as a prerequisite for adopting appropriate input data processing tools. Also, the input satellite bands and the ANN structure (i.e., the number of hidden layers and neurons) should be optimized locally in the desired study area to make sure reliable estimation of water depth and boundary with small uncertainty is reached.

5. Conclusions

The catastrophic drying of the hyper-saline Lake Urmia (LU) has

been recognized as one of the most serious environmental issues of international interest over the past decade. Sustainable restoration of the lake relies heavily on an appropriate understanding of the lake dynamics, which should be monitored continuously to decipher the causal relationship between the lake water volume and its controlling processes. In this study, we used extensive hydrography data and high-resolution satellite imagery to derive three-dimensional water depth and bathymetric maps in the LU at multiple instances between 2017 and 2020. To this end, we developed a machine learning-based model to derive the complex, non-linear relationship between water depth and surface reflectance. The hydrography data included 32,984 points surveyed via six campaigns from September 2017 to May 2010 by the Urmia Lake Restoration Program (ULRP). By processing 172 Landsat images between 1984 and 2020, we further developed the level-area relationship that describes the driest and wettest conditions of the LU in the past 50 years. We found that by clustering in-situ hydrography data and optimizing the number of satellite bands required for the model training purposes, the model accuracy improved significantly. The testing process yielded errors that were much smaller than the lake-averaged water depth as evidence by RMSE = 7.8 ~ 17.9 cm. We also observed that two different linear relationships hold between H and A in the LU, with a threshold behavior at H = 1271.31 m. Our results indicated that no single relationship could describe the changes of lake water volume versus H over a long period. The derived bathymetric maps witnessed remarkable changes in the lakebed topography due to salt precipitation and dissolution during the episodes of lake drying and wetting. Given the highly dynamic relationship between H and volume, the findings of this study highlight the necessity of continuous and frequent bathymetric mapping in the LU. We finally observed that the LU water volume in May 2020 was 3.6 times larger than that in February 2019, indicating a remarkable increase in the rate of lake restoration during this period.

CRediT authorship contribution statement

Mohammad Danesh-Yazdi: Supervision, Conceptualization, Validation, Writing - original draft. **Majid Bayati:** Methodology, Software, Formal analysis, Writing - review & editing. **Massoud Tajrishy:** Validation, Writing - review & editing. **Behdad Chehrenegar:** Writing - review & editing.

Declaration of Competing Interest

The authors declare that they have no known competing financial interests or personal relationships that could have appeared to influence the work reported in this paper.

References

Abbaspour, M., Javid, A.H., Mirbagheri, S.A., Ahmadi Givi, F., Moghimi, P., 2012. Investigation of lake drying attributed to climate change. Int. J. Environ. Sci. Technol. 9 (2), 257–266. https://doi.org/10.1007/s13762-012-0031-0.

AghaKouchak, A., Norouzi, H., Madani, K., Mirchi, A., Azarderakhsh, M., Nazemi, A., Nasrollahi, N., Farahmand, A., Mehran, A., Hasanzadeh, E., 2015. Aral Sea syndrome desiccates Lake Urmia: Call for action. J. Gt. Lakes Res. 41 (1), 307–311. https://doi.org/10.1016/j.jglr.2014.12.007.

Alfakih, A.Y., 2018. Euclidean Distance Matrices and Their Applications in Rigidity Theory. Springer International Publishing, Cham. https://doi.org/10.1007/978-3-319-97846-8.

Amiri, V., Nakhaei, M., Lak, R., Kholghi, M., 2016a. Geophysical, isotopic, and hydrogeochemical tools to identify potential impacts on coastal groundwater resources from Urmia hypersaline Lake, NW Iran. Environ. Sci. Pollut. Res. 23 (16), 16738–16760. https://doi.org/10.1007/s11356-016-6859-y.

Amiri, V., Nakhaei, M., Lak, R., Kholghi, M., 2016b. Assessment of seasonal groundwater quality and potential saltwater intrusion: a study case in Urmia coastal aquifer (NW Iran) using the groundwater quality index (GQI) and hydrochemical facies evolution diagram (HFE-D). Stoch. Environ. Res. Risk Assess. 30 (5), 1473–1484. https://doi.org/10.1007/s00477-015-1108-3.

Amiri, V., Nakhaei, M., Lak, R., Kholghi, M., 2016c. Investigating the salinization and freshening processes of coastal groundwater resources in Urmia aquifer. NW Iran. Environ. Monit. Assess. 188, 233. https://doi.org/10.1007/s10661-016-5231-5.

Arabsahebi, R., Voosoghi, B., Tourian, M.J., 2020. A denoising–classification–retracking method to improve spaceborne estimates of the water level–surface–volume relation over the Urmia Lake in Iran. Int. J. Remote Sens. 41 (2), 506–533. https://doi.org/10.1080/01431161.2019.1643938.

Bayati, M., Danesh-Yazdi, M., 2021. Mapping the spatiotemporal variability of salinity in the hypersaline Lake Urmia using Sentinel-2 and Landsat-8 imagery. J. Hydrol. 595, 126032. https://doi.org/10.1016/j.jhydrol.2021.126032.

Bedford, D., 2009. The Great Salt Lake America's Aral Sea? Environ. Sci. Policy Sustain. Dev. 51 (5), 8–21. https://doi.org/10.3200/ENVT.51.5.8-21.

Benson, L.V., Meyers, P.A., Spencer, R.J., 1991. Change in the size of Walker Lake during the past 5000 years. Palaeogeogr. Palaeoclimatol. Palaeoecol. 81 (3-4), 189–214. https://doi.org/10.1016/0031-0182(91)90147-J.

Bian, X., Shao, Y., Wang, S., Tian, W., Wang, X., Zhang, C., 2018. Shallow Water Depth Retrieval From Multitemporal Sentinel-1 SAR Data. IEEE J. Sel. Top. Appl. Earth Obs. Remote Sens. 11 (9), 2991–3000. https://doi.org/10.1109/JSTARS.2018.2851845.

Caballero, I., Stumpf, R., 2020. Towards Routine Mapping of Shallow Bathymetry in Environments with Variable Turbidity: Contribution of Sentinel-2A/B Satellites Mission. Remote Sens 12 (3), 451. https://doi.org/10.3390/rs12030451.

Cahalane, C., Magee, A., Monteys, X., Casal, G., Hanafin, J., Harris, P., 2019. A comparison of Landsat 8, RapidEye and Pleiades products for improving empirical predictions of satellite-derived bathymetry. Remote Sens. Environ. 233, 111414. https://doi.org/10.1016/j.rse.2019.111414.

Ceyhun, Ö., Yalçın, A., 2010. Remote sensing of water depths in shallow waters via artificial neural networks. Estuar. Coast. Shelf Sci. 89 (1), 89–96. https://doi.org/10.1016/j.ecss.2010.05.015.

Chauvin, Y., Rumelhart, D.E., 1995. Backpropagation: theory, architectures, and applications. Lawrence Erlbaum Associates Inc, Hillsdale, N.J.

Choudhary, A., Rishi, R., Ahlawat, S., Dhaka, V.S., 2010. Performance analysis of feed forward MLP with various activation functions for handwritten numerals recognition. In: 2010 The 2nd International Conference on Computer and Automation Engineering (ICCAE). Presented at the 2nd International Conference on Computer and Automation Engineering (ICCAE 2010), pp. 852–856. https://doi.org/10.1109/ICCAE.2010.5451890.

da Silva, I.N., Andrade Flauzino, R., dos Reis Alves, S.F., Hernane Spatti, D., Liboni, L.H. B., 2017. Artificial Neural Networks: A Practical Course, 1st ed. 2017. ed. Springer International Publishing : Imprint: Springer, Cham. https://doi.org/10.1007/978-3-319-43162-8.

Danesh-yazdi, M., Ataie-Ashtiani, B., 2019. Lake Urmia crisis and restoration plan: planning without appropriate data and model is gambling. J. Hydrol. 576, 639–651. https://doi.org/10.1016/j.jhydrol.2019.06.068.

Dierssen, H.M., Theberge, A.E., 2014. Bathymetry: Assessing Methods. Encycl. Ocean Sci.

Feng, J., Lu, S., 2019. Performance analysis of various activation functions in artificial neural networks. J. Phys. Conf. Ser. 1237, 022030. https://doi.org/10.1088/1742-6596/1237/2/022030.

Feyisa, G.L., Meilby, H., Fensholt, R., Proud, S.R., 2014. Automated Water Extraction Index: A new technique for surface water mapping using Landsat imagery. Remote Sens. Environ. 140, 23–35. https://doi.org/10.1016/j.rse.2013.08.029.

Gao, J., 2009. Bathymetric mapping by means of remote sensing: methods, accuracy and limitations. Prog. Phys. Geogr. Earth Environ. 33 (1), 103–116. https://doi.org/10.1177/0309133309105657.

Gholamalifard, M., Kutser, T., Esmaili-Sari, A., Abkar, A., Naimi, B., 2013. Remotely Sensed Empirical Modeling of Bathymetry in the Southeastern Caspian Sea. Remote Sens. 5, 2746–2762. https://doi.org/10.3390/rs5062746.

Gronewold, A.D., Smith, J.P., Read, L.K., Crooks, J.L., 2020. Reconciling the water balance of large lake systems. Adv. Water Resour. 137, 103505. https://doi.org/10.1016/j.advwatres.2020.103505.

Han, J., Pei, J., Kamber, M., Safari, an O.M.C., 2011. Data Mining: Concepts and Techniques, third ed.

Ilori, C., Pahlevan, N., Knudby, A., 2019. Analyzing Performances of Different Atmospheric Correction Techniques for Landsat 8: Application for Coastal Remote Sensing. Remote Sens. 11, 469. https://doi.org/10.3390/rs11040469.

ISRC, 2018. Technical Report of Depth Assessment and Urmia Lake Bed Profile. Iranian Space Research Center, Iranian Institute of Space Research Mechanics.

Javadzadeh, H., Ataie-Ashtiani, B., Hosseini, S.M., Simmons, C.T., 2020. Interaction of lake-groundwater levels using cross-correlation analysis: A case study of Lake Urmia

Basin. Iran. Sci. Total Environ. 729, 138822. https://doi.org/10.1016/j. scitotenv.2020.138822.

Jawak, S.D., Vadlamani, S.S., Luis, A.J., 2015. A Synoptic Review on Deriving Bathymetry Information Using Remote Sensing Technologies: Models. Methods and Comparisons. Adv. Remote Sens. 04 (02), 147–162. https://doi.org/10.4236/ars.2015.42013.

Jupp, D.L., 1988. Background and extensions to depth of penetration (DOP) mapping in shallow coastal waters. in: Proceeding of The Symposium on Remote Sensing of the Coastal Zone Queensland.

Kabiri, K., 2017. Accuracy assessment of near-shore bathymetry information retrieved from Landsat-8 imagery. Earth Sci. Inform. 10 (2), 235–245. https://doi.org/10.1007/s12145-017-0293-7.

Karimi, N., Bagheri, M.H., Hooshyaripor, F., Farokhnia, A., Sheshangosht, S., 2016. Deriving and Evaluating Bathymetry Maps and Stage Curves for Shallow Lakes Using Remote Sensing Data. Water Resour. Manag. 30 (14), 5003–5020. https://doi.org/10.1007/s11269-016-1465-9.

Klonowski, W.M., 2007. Retrieving key benthic cover types and bathymetry from hyperspectral imagery. J. Appl. Remote Sens. 1 (1), 011505. https://doi.org/10.1117/1.2816113.

Knudby, A., Ahmad, S.K., Ilori, C., 2016. The Potential for Landsat-Based Bathymetry in Canada. Can. J. Remote Sens. 42 (4), 367–378. https://doi.org/10.1080/07038992.2016.1177452.

Kutser, T., Hedley, J., Giardino, C., Roelfsema, C., Brando, V.E., 2020. Remote sensing of shallow waters – A 50 year retrospective and future directions. Remote Sens. Environ. 240, 111619. https://doi.org/10.1016/j.rse.2019.111619.

Lahijani, H.A.K., Rostamabadi, S., Naderi Beni, A., Shirzade, M., Barin, M., 2020. Sediment Distribution Pattern in Lake Urmia, in: The Handbook of Environmental Chemistry. Springer Berlin Heidelberg, Berlin, Heidelberg. https://doi.org/10.1007/698_2020_674.

Landsat collection 2 (Report No. 2021–3002), 2021. Fact Sheet. Reston, VA. https://doi.org/10.3133/fs20213002.

Li, S.Z., Jain, A. (Eds.), 2009. Mahalanobis Distance, in: Encyclopedia of Biometrics. Springer US, Boston, MA, pp. 953–953. https://doi.org/10.1007/978-0-387-73003-5_865.

Li, Y., Gao, H., Jasinski, M.F., Zhang, S., Stoll, J.D., 2019. Deriving High-Resolution Reservoir Bathymetry From ICESat-2 Prototype Photon-Counting Lidar and Landsat Imagery. IEEE Trans. Geosci. Remote Sens. 57 (10), 7883–7893. https://doi.org/10.1109/TGRS.3610.1109/TGRS.2019.2917012.

Likas, A., Vlassis, N., Verbeek, J., 2003. The global k-means clustering algorithm. Pattern Recognit. 36, 451–461. https://doi.org/10.1016/S0031-3203(02)00060-2.

Liu, S., Wang, L., Liu, H., Su, H., Li, X., Zheng, W., 2018. Deriving bathymetry from optical images with a localized neural network algorithm. IEEE Trans. Geosci. Remote Sens. 56 (9), 5334–5342. https://doi.org/10.1109/TGRS.3610.1109/TGRS.2018.2814012.

Lyzenga, D.R., 1985. Shallow-water bathymetry using combined lidar and passive multispectral scanner data. Int. J. Remote Sens. 6 (1), 115–125. https://doi.org/10.1080/01431168508948428.

Lyzenga, D.R., 1978. Passive remote sensing techniques for mapping water depth and bottom features. Appl. Opt. 17 (3), 379. https://doi.org/10.1364/AO.17.000379.

Lyzenga, D.R., Malinas, N.P., Tanis, F.J., 2006. Multispectral bathymetry using a simple physically based algorithm. IEEE Trans. Geosci. Remote Sens. 44 (8), 2251–2259. https://doi.org/10.1109/TGRS.2006.872909.

Ma, Y., Xu, N., Liu, Z., Yang, B., Yang, F., Wang, X.H., Li, S., 2020. Satellite-derived bathymetry using the ICESat-2 lidar and Sentinel-2 imagery datasets. Remote Sens. Environ. 250, 112047. https://doi.org/10.1016/j.rse.2020.112047.

Manaffar, R., Abdolahzadeh, N., MoosaviToomatari, G., Zare, S., Sorgeloos, P., Bossier, P., Van Stappen, G., 2020. Reproduction and life span characterization of Artemia urmiana in Lake Urmia, Iran (Branchiopoda: Anostraca). IFRO 19, 1344–1358.

Manessa, M.D.M., Kanno, A., Sekine, M., Haidar, M., Yamamoto, K., Imai, T., Higuchi, T., 2016. Satellite-Derived Bathymetry Using Random Forest Algorithm and Worldview-2 Imagery. Geoplanning J. Geomat. Plan. 3, 117. https://doi.org/10.14710/geoplanning.3.2.117-126.

Matsushita, B., Fukushima, T., Matsushige, K., Imai, A., Oyama, Y., 2009. Application of spectral decomposition algorithm for mapping water quality in a turbid lake (Lake Kasumigaura, Japan) from Landsat TM data. ISPRS J. Photogramm. Remote Sens. 64 (1), 73–85. https://doi.org/10.1016/j.isprsjprs.2008.04.005.

McFEETERS, S.K., 1996. The use of the Normalized Difference Water Index (NDWI) in the delineation of open water features. Int. J. Remote Sens. 17 (7), 1425–1432. https://doi.org/10.1080/01431169608948714.

Mehr, S.S., Moghaddam, A.A., Field, M.S., 2019. Hydrogeological and geochemical evidence for the origin of brackish groundwater in the Shabestar plain aquifer, northwest Iran. Sustain. Water Resour. Manag. 5 (4), 1381–1404. https://doi.org/10.1007/s40899-017-0192-6.

Micklin, P., 2007. The Aral Sea Disaster. Annu. Rev. Earth Planet. Sci. 35 (1), 47–72. https://doi.org/10.1146/annurev.earth.35.031306.140120.

Micklin, P.P., 1988. Desiccation of the Aral Sea: A Water Management Disaster in the Soviet Union. Science 241 (4870), 1170–1176. https://doi.org/10.1126/science.241.4870.1170.

Misra, A., Vojinovic, Z., Ramakrishnan, B., Luijendijk, A., Ranasinghe, R., 2018. Shallow water bathymetry mapping using Support Vector Machine (SVM) technique and multispectral imagery. Int. J. Remote Sens. 39 (13), 4431–4450. https://doi.org/10.1080/01431161.2017.1421796.

Mohamed, H., AbdelazimNegm, Salah, M., Nadaoka, K., Zahran, M., 2017. Assessment of proposed approaches for bathymetry calculations using multispectral satellite

images in shallow coastal/lake areas: a comparison of five models. Arab. J. Geosci. 10 (2) https://doi.org/10.1007/s12517-016-2803-1.

Mohamed, H., Negm, A., Zahran, M., Saavedra, O.C., 2016. Bathymetry Determination from High Resolution Satellite Imagery Using Ensemble Learning Algorithms in Shallow Lakes: Case Study El-Burullus Lake. Int. J. Environ. Sci. Dev. 7 (4), 295–301. https://doi.org/10.7763/IJESD.2016.V7.787.

Moses, S.A., Janaki, L., Joseph, S., Gomathi, J.P., Joseph, J., 2013. Lake bathymetry from Indian Remote Sensing (P6-LISS III) satellite imagery using artificial neural network model. Lakes Reserv. Res. Manag. 18, 145–153. https://doi.org/10.1111/lre.12027.

Nilsson, K.A., Ross, M.A., Trout, K.E., 2008. Analytic Method to Derive Wetland Stage-Storage Relationships Using GIS Areas. J. Hydrol. Eng. 13 (4), 278–282. https://doi.org/10.1061/(ASCE)1084-0699(2008)13:4(278).

Oyama, Y., Matsushita, B., Fukushima, T., Nagai, T., Imai, A., 2007. new algorithm for estimating chlorophyll-a concentration from multi-spectral satellite data in Case II waters: _ A simulation based on a controlled laboratory experiment. Int. J, Remote Sens.

Pacheco, A., Horta, J., Loureiro, C., Ferreira, Ó., 2015. Retrieval of nearshore bathymetry from Landsat 8 images: A tool for coastal monitoring in shallow waters. Remote Sens. Environ. 159, 102–116. https://doi.org/10.1016/j.rse.2014.12.004.

Sadeghi-Bazargani, H., Allahverdipour, H., Asghari Jafarabadi, M., Azami-Aghdash, S., 2019. Lakes Drying and Their Adverse Effects on Human Health: A Systematic Review. Iran. J. Public Health 48, 227–237.

Saemian, P., Elmi, O., Vishwakarma, B.D., Tourian, M.J., Sneeuw, N., 2020. Analyzing the Lake Urmia restoration progress using ground-based and spaceborne observations. Sci. Total Environ. 739, 139857. https://doi.org/10.1016/j.scitotenv.2020.139857.

Safavi, S., Saghafian, B., Hosseini, S.A., 2020. Characterizing flow pattern and salinity using the 3D MIKE 3 model: Urmia Lake case study. Arab. J. Geosci. 13, 115. https://doi.org/10.1007/s12517-020-5095-4.

Sagawa, T., Yamashita, Y., Okumura, T., Yamanokuchi, T., 2019. Satellite derived bathymetry using machine learning and multi-temporal satellite images. Remote Sens. 11, 1155. https://doi.org/10.3390/rs11101155.

Sandidge, J.C., Holyer, R.J., 1998. Coastal Bathymetry from Hyperspectral Observations of Water Radiance. Remote Sens. Environ. 65 (3), 341–352. https://doi.org/10.1016/S0034-4257(98)00043-1.

Sharifi, A., Shah-Hosseini, M., Pourmand, A., Esfahaninejad, M., Haeri-Ardakani, O., 2018. The Vanishing of Urmia Lake: A Geolimnological Perspective on the Hydrological Imbalance of the World's Second Largest Hypersaline Lake. In: The Handbook of Environmental Chemistry. Springer, Berlin Heidelberg, Berlin, Heidelberg. https://doi.org/10.1007/698_2018_359.

Sheibani, S., Ataie-Ashtiani, B., Safaie, A., Simmons, C.T., 2020. Influence of lakebed sediment deposit on the interaction of hypersaline lake and groundwater: A simplified case of lake Urmia. Iran. J. Hydrol. 588, 125110. https://doi.org/10.1016/j.jhydrol.2020.125110.

Shen, F., Suhyb Salama, MHD., Zhou, Y.-X., Li, J.-F., Su, Z., Kuang, D.-B., 2010. Remote-sensing reflectance characteristics of highly turbid estuarine waters – a comparative experiment of the Yangtze River and the Yellow River. Int. J. Remote Sens. 31 (10), 2639–2654. https://doi.org/10.1080/01431160903085610.

Sima, S., Tajrishy, M., 2013. Using satellite data to extract volume – area – elevation relationships for Urmia Lake. Iran. J. Gt. Lakes Res. 39 (1), 90–99. https://doi.org/10.1016/j.jglr.2012.12.013.

Smith, W.H.F., Sandwell, D.T., 1994. Bathymetric prediction from dense satellite altimetry and sparse shipboard bathymetry. J. Geophys. Res. Solid Earth 99 (B11), 21803–21824. https://doi.org/10.1029/94JB00988.

Smith, W.H.F., Sandwell, D.T., Raney, R.K., 2005. Bathymetry From Satellite Altimetry: Present And Future, in: Proceedings of OCEANS 2005 MTS/IEEE. Presented at the OCEANS 2005 MTS/IEEE, IEEE, Washington, DC, USA, pp. 1–4. https://doi.org/10.1109/OCEANS.2005.1640160.

Stenger-Kovács, C., Lengyel, E., Buczkó, K., Tóth, F., Crossetti, L., Pellinger, A., Zámbóné Doma, Z., Padisák, J., 2014. Vanishing world: alkaline, saline lakes in Central Europe and their diatom assemblages. Inland Waters 4 (4), 383–396. https://doi.org/10.5268/IW10.5268/IW-4.4.010.5268/IW-4.4.722.

Stewart, C., Renga, A., Gaffney, V., Schiavon, G., 2016. Sentinel-1 bathymetry for North Sea palaeolandscape analysis. Int. J. Remote Sens. 37 (3), 471–491. https://doi.org/10.1080/01431161.2015.1129563.

Stumpf, R.P., Holderied, K., Sinclair, M., 2003. Determination of water depth with high-resolution satellite imagery over variable bottom types. Limnol. Oceanogr. 48 (1part2), 547–556. https://doi.org/10.4319/lo.2003.48.1_part_2.0547.

Sun, W., Du, B., Xiong, S., 2017. Quantifying Sub-Pixel Surface Water Coverage in Urban Environments Using Low-Albedo Fraction from Landsat Imagery. Remote Sens. 9, 428. https://doi.org/10.3390/rs9050428.

Tourian, M.J., Elmi, O., Chen, Q., Devaraju, B., Roohi, S., Sneeuw, N., 2015. A spaceborne multisensor approach to monitor the desiccation of Lake Urmia in Iran. Remote Sens. Environ. 156, 349–360. https://doi.org/10.1016/j.rse.2014.10.006.

Urmia Lake Restoration Program, 2018. Urmia Lake: Lessons and Challenges.

Vaheddoost, B., Aksoy, H., 2018. Interaction of groundwater with Lake Urmia in Iran. Hydrol. Process. https://doi.org/10.1002/hyp.13263.

Vaheddoost, B., Aksoy, H., Abghari, H., Naghadeh, S.Z., 2015. Decision Tree for Measuring the Interaction of Hyper-Saline Lake and Coastal Aquifer in Lake Urmia. In: Watershed Management 2015. Presented at the Watershed Management Symposium 2015. American Society of Civil Engineers, Reston, VA, pp. 62–71. https://doi.org/10.1061/9780784479322.006.

Vanhellemont, Q., 2019. Adaptation of the dark spectrum fitting atmospheric correction for aquatic applications of the Landsat and Sentinel-2 archives. Remote Sens. Environ. 225, 175–192. https://doi.org/10.1016/j.rse.2019.03.010.

Vanhellemont, Q., Ruddick, K., 2014. Turbid wakes associated with offshore wind turbines observed with Landsat 8. Remote Sens. Environ. 145, 105–115. https://doi.org/10.1016/j.rse.2014.01.009.

Wang, L., Liu, H., Su, H., Wang, J., 2019. Bathymetry retrieval from optical images with spatially distributed support vector machines. GIScience Remote Sens. 56 (3), 323–337. https://doi.org/10.1080/15481603.2018.1538620.

Water Research Institute, 2015. Deriving the bathymetric map of the Lake Urmia and estimating the salt precipitation rate between 2013 and 2015 using field measurements and remote sensing data. Iran Water and Power Resources Development Company.

Wei, J., Lee, Z., Garcia, R., Zoffoli, L., Armstrong, R.A., Shang, Z., Sheldon, P., Chen, R.F., 2018. An assessment of Landsat-8 atmospheric correction schemes and remote sensing reflectance products in coral reefs and coastal turbid waters. Remote Sens. Environ. 215, 18–32. https://doi.org/10.1016/j.rse.2018.05.033.

Winter, T.C., 1981. Uncertainties in Estimating the Water Balance of Lakes. J. Am. Water Resour. Assoc. 17 (1), 82–115. https://doi.org/10.1111/j.1752-1688.1981.tb02593.x.

Wurtsbaugh, W.A., Miller, C., Null, S.E., DeRose, R.J., Wilcock, P., Hahnenberger, M., Howe, F., Moore, J., 2017. Decline of the world's saline lakes. Nat. Geosci. 10 (11), 816–821. https://doi.org/10.1038/ngeo3052.

Xu, H., 2006. Modification of normalised difference water index (NDWI) to enhance open water features in remotely sensed imagery. Int. J. Remote Sens. 27 (14), 3025–3033. https://doi.org/10.1080/01431160600589179.

Xu, N., Ma, Y., Zhou, H., Zhang, W., Zhang, Z., Wang, X.H., 2020. A Method to Derive Bathymetry for Dynamic Water Bodies Using ICESat-2 and GSWD Data Sets. IEEE Geosci. Remote Sens. Lett. 1–5 https://doi.org/10.1109/LGRS.2020.3019396.

Yunus, A.P., Dou, J., Song, X., Avtar, R., 2019. Improved Bathymetric Mapping of Coastal and Lake Environments Using Sentinel-2 and Landsat-8 Images. Sensors 19, 2788. https://doi.org/10.3390/s19122788.

Zeinoddini, M., Tofighi, M.A., Vafaee, F., 2009. Evaluation of dike-type causeway impacts on the flow and salinity regimes in Urmia Lake. Iran. J. Gt. Lakes Res. 35 (1), 13–22. https://doi.org/10.1016/j.jglr.2008.08.001.